2019

Nonlinear Control Synthesis for Facilitation of Human-Robot Interaction

Zhangchi Ding
University of Central Florida

NONLINEAR CONTROL SYNTHESIS FOR FACILITATION OF HUMAN-ROBOT INTERACTION

by

ZHANGCHI DING
M.S. University of Central Florida, 2016
B.S. Shenzhen University, 2013

A dissertation submitted in partial fulfilment of the requirements
for the degree of Doctor of Philosophy
in the Department of Electrical and Computer Engineering
in the College of Engineering and Computer Science
at the University of Central Florida
Orlando, Florida

Fall Term
2019

Major Professor: Aman Behal

ABSTRACT

Human-robot interaction is an area of interest that is becoming increasingly important in robotics research. Nonlinear control design techniques allow researchers to guarantee stability, performance, as well as safety, especially in cases involving physical human-robot interaction (PHRI). In this dissertation, we will propose two different nonlinear controllers and detail the design of an assistive robotic system to facilitate human-robot interaction.

In Chapter 2, to facilitate physical human-robot interaction, the problem of making a safe compliant contact between a human and an assistive robot is considered. Users with disabilities have a need to utilize their assistive robots for physical interaction during activities such as hair-grooming, scratching, face-sponging, etc. Specifically, we propose a hybrid force/velocity/attitude control for our physical human-robot interaction system which is based on measurements from a force/torque sensor mounted on the robot wrist. While automatically aligning the end-effector surface with the unknown environmental (human) surface, a desired commanded force is applied in the normal direction while following desired velocity commands in the tangential directions. A Lyapunov based stability analysis is provided to prove both convergence as well as passivity of the interaction to ensure both performance and safety. Simulation as well as experimental results verify the performance and robustness of the proposed hybrid force/velocity/attitude controller in the presence of dynamic uncertainties as well as safety compliance of human-robot interactions for a redundant robot manipulator.

Chapter 3 presents the design, analysis, and experimental implementation of an adaptive control enabled intelligent algorithm to facilitate 1-click grasping of novel objects by a robotic gripper since one of the most common types of tasks for an assistive robot is pick and place/object retrieval tasks. But there are a variety of objects in our daily life all of which need different optimal force to grasp them. This algorithm facilitates automated grasping force adjustment. The use

of object-geometry free modeling coupled with utilization of interaction force and slip velocity measurements allows for the design of an adaptive backstepping controller that is shown to be asymptotically stable via a Lyapunov-based analysis. Experiments with multiple objects using a prototype gripper with embedded sensing show that the proposed scheme is able to effectively immobilize novel objects within the gripper fingers. Furthermore, it is seen that the adaptation allows for close estimation of the minimum grasp force required for safe grasping which results in minimal deformation of the grasped object.

In Chapter 4, we present the design and implementation of the motion controller and adaptive interface for the second generation of the UCF-MANUS intelligent assistive robotic manipulator system. Based on usability testing for the system, several features were implemented in the interface that could reduce the complexity of the human-robot interaction while also compensating for the deficits in different human factors, such as Working Memory, Response Inhibition, Processing Speed; , Depth Perception, Spatial Ability, Contrast Sensitivity. For the controller part, we designed several new features to provide the user has a less complex and safer interaction with the robot, such as 'One-click mode', 'Move suggestion mode' and 'Gripper Control Assistant'. As for the adaptive interface design, we designed and implemented compensators such as 'Contrast Enhancement', 'Object Proximity Velocity Reduction' and 'Orientation Indicator'.

To my wife Xuan and my parents.

ACKNOWLEDGMENTS

First of all, I want to express my sincere gratitude to my advisor Dr. Aman Behal, for his insightful guidance, patience and motivation. The countless hours he spent with me discussing different problems and sharing his immense knowledge have had a great influence on my research life. Besides my advisor, I also want to thank the rest of my dissertation committee members: Dr. Ladislau Boloni, Dr. Michael Haralambous, Dr. Yunjun Xu, and Dr. Yaser P. Fallah, for their insightful comments and valuable time. I would also like to thank all my group-mates for their generous and invaluable help during the course of my work at the UCF Assistive Robotics Laboratory. Finally, I would like to thank my wife Xuan and my parents for all the love, support and undiminishing faith in me.

TABLE OF CONTENTS

LIST OF FIGURES

LIST OF TABLES

CHAPTER 1: INTRODUCTION

With the latest advances in the field of robotics, the robot manipulator is being utilized increasingly outside the caged industrial environment that it was initially developed for. Professional and personal service robots are increasingly working with humans in their daily lives at work and at home. One class of personal service robots is assistive robotics which is the field of robotics meant to assist users with activities of daily living. These may be aging users who are weak and easily fatigued or individuals with disabilities that may have trouble with control in the upper and/or lower extremities. It is well know from previous research that users of assistive robotics prefer to have the ability to interact with a robot especially because robots are not as context and situation aware as their human counterparts even though they may be more consistent in interactions with environments that they are specifically trained for. However, the control of a robot manipulator is very different from the control of a human arm. Human can easily move all the joints of the arm with respect to a target simultaneously. Take the shaving task for example, the wrist can align the razor with face while the razor is moving along the face. If this task is to be done through a robot, manual control is almost impossible to achieve during human-robot interaction since the robot usually can only be commanded to move each joint or axis separately, while these physical human-robot interaction tasks need the motion in different axes simultaneously. Furthermore, even for tasks such as object retrieval/pick-and-place, standard user interfaces do not allow for efficient motion of the robot end-effector toward the target and the eventual application of optimal force(s) to safely immobilize the object within the robot gripper. To facilitate such human-robot interaction problems, we propose and design two nonlinear controller as well as implement an intelligent assistive robotic system, namely the UCF-MANUS Gen 2 system.

In Chapter 2, a physical human-robot interaction is considered. While assistive robotic devices such as Wheelchair Mounted Robotic Arms (WMRAs) [1–5] and Companion Robots [6–10] tradi-

tionally help users with object retrieval [49] or pick and place tasks [12], they are also quite capable of physical interaction with the user themselves. Users with disabilities have a need for assistance with activities such hair-grooming, scratching, face-sponging etc.; all these daily activities require physical interaction with various surfaces on the human body. Under this need, the assistive robot has to be able to align with the unknown (human) surface, and also apply a desired force in the normal direction while following the surface based on desired velocity profiles that the user can command to the robot. It is critical that the assistive robot be able to execute a safe compliant contact with the human user.

In Chapter 3, an adaptive grasping force control algorithm is presented. To assist the human to achieve daily activities, the ability to appropriately grasp an object is essential for most robotic manipulators. There can exist a large variation between the different objects that a robot is required to grasp which makes the grasping problem complicated. It becomes even more challenging in unstructured scenarios, i.e., when the robot has no previous knowledge of the object's shape or size. If the robot grasps an object too loosely, it will be unable to pick the object or lose it during transit; on the other hand, too tight a grasp can inadvertently crush or damage some objects. Even when an object is previously known, it is hard to distinguish its true state without interacting with it, e.g., an empty versus full soda can. The requirement for successful grasping thus boils down to the application of a minimal force which immobilizes the object between the gripper fingers, i.e., no slip must be ensured between the object and gripper fingers.

In Chapter 4, the UCF-MANUS assistive robot system is presented. The UCF-MANUS assistive are aimed at compensating for limits in the cognitive and/or motor functions of user such as helping wheelchair-bound individuals retrieve objects in their environment, feed themselves, and so on. Based on our previous research, we have found users prefer more interaction with the robot rather than the cede control to autonomous functions by the robot. Based on this, we are motivated to design a shared control framework for assistive robots. The users can always take over robot con-

trol function or share workload with the robot's software agent that is imbued with autonomy and exhibits situational awareness; in other words, collaborative control with sliding scale autonomy allows for reduction of task complexity.

CHAPTER 2: ROBUST HYBRID IMPEDANCE CONTROL FOR PHYSICAL HUMAN ROBOT INTERACTION (P-HRI)

Background

To achieve the hybrid position/force control on surface, researchers have proposed various ways to solve it. In [13],the author used the exact CAD model for polishing position/force control. With the CAD/CAM model, they are able to track the desired trajectory, force, and contact direction. Since it requires the exact CAD model of the environment, therefore this method will not works will for the physcial human-robot interaction problem. In [14],the authors designed and implemented a compliant arm to perform bed bath for patient hygiene. A bang-bang controller was utilized to maintain the z-axis force against the body between 1-3N while a laser range finder was utilized to retrieve the skin surface point cloud of the skin followed by selection of wiping area by the operator. This method also required to obtain the point cloud of the environment. The authors of [15] proposed a contact force model for wiping and shaving tasks. They captured the face point cloud and the force profile of health participants performing daily living tasks such as wiping and shaving. Then, they built a three-parameter trapezoidal force model of each stroke and the force dependency on face area. Besides assuming previous knowledge of the environment, there are other approaches for the unknown environment. In [16], the author proposed two methods for exploring unknown surfaces with discontinuities by using only a force/torque sensor. They rotating the direction of the desired motion/force instead of rotating the end-effector to keep moving and inserting force on unknown surface. But this method can't be used for certain physical human-robot interaction which needs the alignment between the end-tool and human body, such as shaving. In [17], the authors proposed a hybrid position-force sliding mode control for surface treatment such as polishing, grinding, finishing, and deburring – the end-effector can apply the desired pres-

sure on the surface and also keep the end-effector orientation perpendicular to the surface. But the orientation constrain is not considered for moving along a frictional environment. In [18],the author proposed a deformation-tracking impedance control for interacting with unknown surfaces by using an extended Kalman filter to estimate the parameters of the environment, thereby controlling the interaction force indirectly by tracking the desired deformation without force sensing. But this method can't estimate the interaction torque, therefore during the aligning phase of the assembly task, their desired interaction torque is just determined experimentaly. In [19], an artificial neural network-based proportional-integral gain scheduling force controller was proposed to track the desire interaction force while estimating the environment parameter online. In [20], the author proposed an inverse differential kinematic based position/force control for cleaning an unknown surface. They utilized a force/torque sensor to provide feedback for the force control part. However, this velocity control-based algorithm is not considered safe for human-robot interaction; furthermore, the evaluation of surface alignment is also missing.

Problem statement

The research objective is to align the robot end-effector with the unknown environment and apply a desired force in the normal direction while following a commanded velocity profile along the tangential directions. In order to guarantee safe human-robot interaction, another research objective is to ensure that the robot acts as a passive system while transmitting user intent to and during interaction with the environment. To design and implement our robust impedance control framework, we assume knowledge of the joint position/velocity measurements as well as the interaction force at the end-effector using a wrist mounted 6-axis force/torque sensor. We assume uncertainty in the robot dynamics and no prior knowledge of the location/orientation of the environmental surface with respect to the robot coordinate system. While we assume that the surface presents

damping and stiffness in the normal direction and pure damping along the surface, we assume no prior knowledge of the parameters.

Modeling

Manipulator Model

The dynamics of an n degree-of-freedom robot are given by

$$M(q)\ddot{q} + C(q,\dot{q})\dot{q} + G(q) = \tau + \tau_{env} - \tau_f \tag{2.1}$$

where $M(q) \in \mathbb{R}^{n\times n}$ is the symmetric positive definite inertia matrix, $C(q,\dot{q}) \in \mathbb{R}^{n\times n}$ is the matrix of Coriolis and centrifugal torques, $G(q) \in \mathbb{R}^{n\times 1}$ is the vector of gravitational torques, $q, \dot{q}, \ddot{q} \in \mathbb{R}^{n\times 1}$ denote, respectively, the joint angle, joint velocity and joint acceleration vectors, $\tau \in \mathbb{R}^{6\times 1}$ is the control input vector of joint torques, $\tau_{env} = J^T F_{e,e} \in \mathbb{R}^{6\times 1}$ is the external torque registered at the robot joints, $F_{e,e} \triangleq \begin{bmatrix} f_{e,e} \end{bmatrix}^T = \begin{bmatrix} f_{e,x} & f_{e,y} & f_{e,z} & \tau_{e,x} & \tau_{e,y} & \tau_{e,z} \end{bmatrix}^T \in \mathbb{R}^{6\times 1}$ is the interaction force measured by the force/torque sensor mounted on the wrist, $J \in \mathbb{R}^{6\times n}$ is the Jacobian matrix, while $\tau_f \in \mathbb{R}^{6\times 1}$ denotes joint friction. The joint velocity and acceleration for a redundant robot (*i.e.,* $n > 6$) can be written as follows

$$\dot{q} = J^+\dot{x} + (I - J^+J)b \tag{2.2}$$

$$\ddot{q} = J^+\ddot{x} - J^+\dot{J}J^+\dot{x} - J^+\dot{J}(I - J^+J)b \tag{2.3}$$

where $\dot{x} = \begin{bmatrix} v_b^T & \omega_b^T \end{bmatrix}^T, \ddot{x} = \begin{bmatrix} \dot{v}_b^T & \dot{\omega}_b^T \end{bmatrix}^T \in \mathbb{R}^{6\times 1}$ denote end-effector velocity and acceleration vectors, respectively, v_b and ω_b are the end-effector translation and angular velocity expressed

in the base frame, $J^+ \triangleq J^T(JJ^T)^{-1}$ denotes the right pseudoinverse of the Jacobian matrix, while $b \in \mathbb{R}^n$ is an arbitrary vector utilized to accomplish secondary objectives such as joint limit, collision avoidance, *etc.* For ease of presentation, we choose $b = 0$ for the remainder of the paper. After replacing the joint acceleration and velocity by (2.2) and (2.3), we can obtain the task space robot dynamics as follows

$$MJ^+\ddot{x} - MJ^+\dot{J}J^+\dot{x} + CJ^+\dot{x} + G - J^T f_{e,e} + \tau_f = \tau \tag{2.4}$$

To accomplish our tangential velocity tracking objectives, we define errors in the end-effector frame as follows

$$e_v = \dot{x}_e - v_d \tag{2.5}$$

where $v_d(t) \triangleq \begin{bmatrix} v_{d,x}(t) & v_{d,y}(t) & 0 & 0 & 0 & 0 \end{bmatrix}^T \in \mathbb{R}^{6\times 1}$ denotes the desired velocity in the end-effector frame, $\dot{x}_e = R^T\dot{x} = \begin{bmatrix} v_e & \omega_e \end{bmatrix}$ denotes the actual end effector velocity expressed in the end-effector frame, $v_e = [\ v_{e,x} \quad v_{e,y} \quad v_{e,z}\ ]^T$ and $\omega_e = [\ \omega_{e,x} \quad \omega_{e,y} \quad \omega_{e,z}\ ]^T$ are the end-effector translation and angular velocity expressed in the end-effector frame, $R \triangleq \begin{bmatrix} R_e^b & 0 \\ 0 & R_e^b \end{bmatrix}$,while $R_e^b(t) \in SO(3)$ denotes the rotation matrix between the robot base frame and the end-effector frame. By rearranging (2.5) and taking its time derivative, one can obtain the following expressions for $\dot{x}(t)$ and $\ddot{x}(t)$

$$\dot{x} = Re_v + Rv_d \tag{2.6}$$

$$\ddot{x} = R\dot{e}_v + R\dot{v}_d + \dot{R}e_v + \dot{R}v_d \tag{2.7}$$

By substituting (2.6) and (2.7) in (2.4), we can obtain the open-loop error dynamics as follows

$$M J^{+} R \dot{e}_{v} = \tau + \tau_{env} - \tau_{f} - G + H \dot{x} - M J^{+} R \dot{v}_{d} \tag{2.8}$$

where $H \triangleq M J^{+} \dot{J} J^{+} - C J^{+} - M J^{+} \dot{R} R^{T}$. We can model the unstructured uncertainties in the robot dynamics as follows

$$M = \hat{M} + \tilde{M} \qquad H = \hat{H} + \tilde{H}$$
$$G = \hat{G} + \tilde{G}$$

where $\hat{M}, \hat{H}, \hat{G}$ denote best estimates of M, H, G respectively while $\tilde{M}, \tilde{H}, \tilde{G}$ denote the corresponding uncertainties. Based on this, we can rewrite the open-loop error dynamcis as follows

$$\hat{M} J^{+} R \dot{e}_{v} = \tau + \tau_{env} - \hat{G} + \hat{H} \dot{x} - \hat{M} J^{+} R \dot{v}_{d} + \hat{M} D \tag{2.9}$$

where $D \triangleq \hat{M}^{-1}(-\tilde{G} + \tilde{H} \dot{x} - \tilde{M} J^{+} R \dot{v}_{d} - \tau_{f})$ is a lumped disturbance term. Motivated by the structure of the robot dynamics and the ensuing control development and stability analysis, we assume the existence of the following properties:

Property 1 All kinematic singularities are always avoided and the inverse of the manipulator Jacobian denoted by $J^{+}(q)$, is assumed to always exist.

Property 2 The actual value and best estimate value of M, G, H are always bounded by a positive constant, such that $\|M\| \leq b_{M}, \|G\| \leq b_{G}, \|H\| \leq b_{H0} + b_{H1} \|\dot{q}\|, \left\|\hat{M}\right\| \leq b_{\hat{M}}, \left\|\hat{G}\right\| \leq b_{\hat{G}}, \left\|\hat{H}\right\| \leq b_{\hat{H}0} + b_{\hat{H}1} \|\dot{q}\|$.

Property 3 The lumped disturbance D is bounded by a function of joint velocity [23] such that $\|D\| < b_{D0} + b_{D1} \|\dot{q}\| + b_{D2} \|\dot{q}\|^{2}$.

Property 4 The end-effector initial orientation is pointing to the environment, such that the end-

effector will make contact with the environment.

Environment Model

We model the environment as a spring-damper which provides the environmental force in object (environment) frame as follow

$$f_{e,o} = K_e(x_n - x_o) + B_e v_o \tag{2.10}$$

where $K_e = \mathrm{diag}[\ 0 \quad 0 \quad k_e\ ], B_e = \mathrm{diag}[\ b_e \quad b_e \quad 0\ ] \in \mathbb{R}^{3\times3}$ are diagonal matrices of the environment stiffness and damping, while $x_n \in \mathbb{R}$ is the z-axis neutral position of the environment in the object frame, $x_o \in \mathbb{R}^{1\times1}$ is the z-axis position of the end-effector position expressed in the object frame, $v_o = R_e^o v_e$ is the interaction velocity between the end-effector and the object, v_e is the end-effector translational velocity as defined earlier, R_o^e is the unknown rotation matrix between the object frame and end-effector frame. In the end-effector frame, the environmental torque in end-effector frame can be defined as follow

$$\tau_e = r_e \times f_{e,e} \tag{2.11}$$

where r_e is the unknown position vector from the center of the sensor to the contact point while $f_{e,e} = R_o^e f_{e,o}$ is the environment force expressed in the end-effector frame. The model of the interaction between the end effector and the environment is shown in Figure 2.1.

We also model the end-tool for the manipulator as a rigid partial sphere as specified in Figure 2.2. In the figure, x_{ee} denotes the center of the robot wrist where the 6-axis force/torque sensor is mounted, x_c denotes the center of the sphere, r_R is the position vector from the sphere center of the end-tool to the contact point, while r_{off} is the position vector from the sphere center to the robot

wrist center and is parallel with the end-effector z-axis denoted by $\hat{z}_e$.

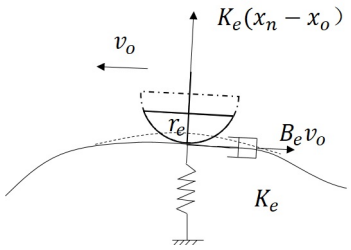

Figure 2.1: Spring-Damper environmental model.

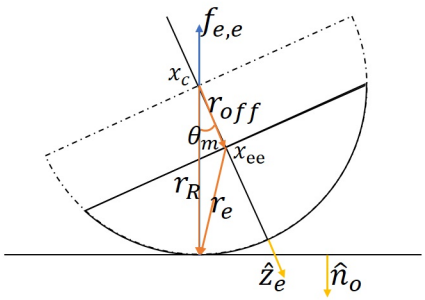

Figure 2.2: End-tool geometry. The end-tool is a partial sphere, x_{ee} is the position of the end-effector and the center of the sensor, x_c is the center of the sphere, r_R is the position vector starts from the sepheire center of the end-tool to the contact point. r_{off} is the position vector starts from the sepheire center to the rotation center, and it parrale with the end-effector z axis.

Control Design and Stability Analysis for Frictionless Environment

Control Design

The proposed control design has an inner loop and an outer loop. While the inner loop is a robust controller to compensate for the system uncertainties and linearize the robot dynamics, the outer loop reshapes the linearized dynamics to the desired dynamics. In what follows, we discuss the design of control strategies within the two loops that guarantees robust stability, convergence, as well as passivity.

Design of the inner loop

Based on the structure of the open-loop error dynamics in (2.8) and our desire to obtain an impedance controller, we first design a computed torque inner loop controller to linearize the dynamics as follows

$$\tau = \hat{M} a_j - \tau_{env} + \hat{G} - \hat{H}\dot{x} + \hat{M} J^{+} R \dot{v}_d \tag{2.12}$$

By substituting (2.12) into (2.9), we can obtain

$$J^{+} R \dot{e}_v = a_j - D \tag{2.13}$$

In (2.12), a_j is an auxiliary control term that is designed to compensate for the disturbance using a sliding mode controller as follows

$$a_j = J^{+} a_x - Q\mathrm{sign}(S) \tag{2.14}$$

where $a_x \triangleq [\ a_{x,v} \quad a_{x,\omega}\ ]^T$ where $a_{x,v}$, $a_{x,\omega}$ are yet to be designed auxiliary control terms which are related to the desired dynamics, Q is the gain for the $\mathtt{sign}()$ (the standard signum) function. Inspired by [23], we design $Q = b_{D0} + b_{D1}\|\dot{q}\| + b_{D2}\|\dot{q}\|^2 + \alpha$, where α is a positive constant, while In (2.14), S denotes a sliding surface which is defined as follows

$$S \triangleq \dot{q} + \int_0^t J^+ \left(\dot{J}J^+\dot{x} - \dot{R}v_e - R\dot{v}_d - \dot{R}v_d - a_x\right) dt \tag{2.15}$$

such that

$$\dot{S} = J^+(R\dot{e}_v - a_x) \tag{2.16}$$

Then we can have following result for the inner loop:

Lemma 2.0.1. *Consider the robot system in (2.8) under the control law of (2.12) and (2.14), the sliding surface S and the derivative of sliding surface $\dot{S}$ will converge to zero in finite time t_1, and remain there in subsequent time, such that* $\lim_{t\to t_1} S = 0$, $\lim_{t\to t_1} \dot{S} = 0$.

Proof. We define a positive-definite function V_S as follows

$$V_S = \frac{1}{2}S^TS \tag{2.17}$$

After time differentiating (2.17) and utilizing (2.16), (2.13), and (2.14), we can obtain

$$\begin{aligned} \dot{V}_S &= S^T(-D - Q\mathtt{sign}(S)) && (2.18)\\ &\leq -(Q - b_{D0} + b_{D1}\|\dot{q}\| + b_{D2}\|\dot{q}\|^2)\|S\| \\ &\leq -\alpha\|S\| \leq 0 && (2.19) \end{aligned}$$

Since sliding mode control [22] has a finite convergence time t_1, then we can have $\lim_{t \to t_1} S = 0$, $\lim_{t \to t_1} \dot{S} = J^{+} R \dot{e}_v - J^{+} a_x = 0$. □

Design of the Desired Dynamics

To finalize the controller design, we first designed our desired dynamics in translational axis as follow

$$M_d \dot{e}_v + B_d e_v + K_d \int e_v = e_f. \tag{2.20}$$

where $M_d \triangleq diag\{m_{d,xy}, m_{d,xy}, m_{d,z}\}$, $B_d \triangleq diag\{b_{d,xy}, b_{d,xy}, b_{d,z}\}$, $K_d \triangleq diag\{k_{d,xy}, k_{d,xy}, 0\}$ denote the desired mass, damping, and stiffness matrices, all elements in the matrices are positive constants, and $e_f \triangleq [\ 0 \quad 0 \quad f_{e,z} - f_{d,z}\ ]$ denotes the force error. Then we design the auxiliary control term $a_{x,v}$ as follow

$$a_{x,v} = R\{M_d^{-1}[-B_d e_v - K_d \int e_v + e_f] + \dot{v}_d\} \tag{2.21}$$

For the angular axis, we designed a quaternion based control to align the end-effector with the unknown environment. The quaternion between the end-effector Z axis $\hat{z}_e$ and environment normal $\hat{n}_o$ can be extract from the torque and force feedback as follow.

Based on the definition of the environment torque (2.11) and the geometry of the end-tool in Figure (2.2), we can rewrite the environment torque as follow

$$\begin{aligned} \tau_e &= r_e \times f_{e,e} \\ &= (R_o^e r_R - r_{off}) f_{e,e} \end{aligned} \tag{2.22}$$

Since there is no friction on the environment surface, based on the geometry of the end tool, we can have $R_o^e r_R // f_{e,e} // \hat{n}_o$, $r_{off} // \hat{z}_e$. Then we can simplify the environmental torque as follow

$$\begin{aligned} \tau_e &= f_{e,e} \times r_{off} \\ &= \|f_{e,e}\| \, \|r_{off}\| \, \hat{n}_o \times \hat{z}_e \end{aligned} \tag{2.23}$$

such that we can find that the direction of the environmental torque vector is parallel with the cross product between $\hat{n}_o$ and $\hat{z}_e$. Then we can calculate the rotation axis n such that

$$n = -\frac{\hat{n}_o \times \hat{z}_e}{\|\hat{n}_o \times \hat{z}_e\|} = -\frac{\tau_e}{\|\tau_e\|} \tag{2.24}$$

Since the rotation direction is already contains in vector n, then the range of the angle θ_m between $\hat{n}_o$ and $\hat{z}_e$ is $[0, \frac{\pi}{2})$. And according to the definition of torque, if we have the length of r_{off}, then we can calculate the angle θ_m between $\hat{n}_o$ and $\hat{z}_e$

$$\theta_m = \arcsin\left(\frac{\|\tau_e\|}{\|f_{e,e}\| \, \|r_{off}\|}\right) \tag{2.25}$$

Since we only have the measurement of τ_e and $f_{e,e}$, then we can only have the value of $\|r_{off}\| \sin(\theta_m)$. Therefore we normalized the $\|r_{off}\|$ with a bigger value of $\|r_M\|$, we can have

$$k \sin(\theta_m) \triangleq \frac{\|\tau_e\|}{\|f_{e,e}\| \, \|r_M\|} \tag{2.26}$$

where $k \triangleq \frac{\|r_{off}\|}{\|r_M\|} \in (0, 1]$ is a positive constant. Then we define $\acute{\theta}_m \triangleq \arcsin(k \sin(\theta_m))$, and we can define the unit quaternion $q(q, q_0)$ based on $n, \acute{\theta}_m$, as follow

$$q_0 = \cos\left(\frac{\acute{\theta}_m}{2}\right), \; q = \sin\left(\frac{\acute{\theta}_m}{2}\right) n$$

And the dynamics of the quaternion $q(q, q_0)$ are as follows

$$\begin{aligned} \dot{q}_0 &= -\tfrac{1}{2}\omega_e^T q \\ \dot{q} &= \tfrac{1}{2}(q_0\omega_e + q \times \omega_e) \end{aligned} \tag{2.27}$$

After we have the quaternion $q(q, q_0)$ which related to the alignment between $\hat{n}_o$ and $\hat{z}_e$, then we can design the desired dynamics in angular axis as follow

$$I_d\dot{\omega}_e + B_{d,\omega}\omega_e = \tau_a \tag{2.28}$$

where $I_d \triangleq diag\{I_{d,x}, I_{d,y}, I_{d,z}\}$, $B_{d,\omega} = \frac{1}{2}(q_0 I_d K_1 + 4P + [q]_\times)$ is a positive varying damping, $\tau_a = -(K_1 - I)q$ is the auxiliary torque, P and K_1 are positive definite diagonal matrix. Then we design the auxiliary control term $a_{x,\omega}$ as follows

$$a_{x,\omega} = RI_d^{-1}[\tau_a - B_{d,\omega}\omega_e] \tag{2.29}$$

The overall proposed controller is shown in Figure 2.3.

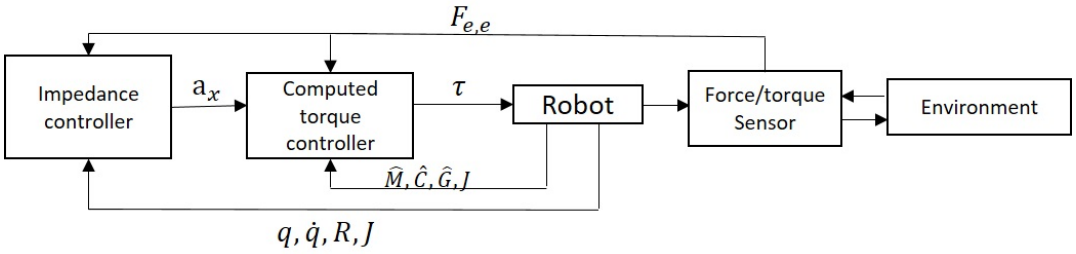

Figure 2.3: Block diagram of the proposed controller.

Stability Analysis

Before presenting the main results, we state the following lemmas which will be invoked later.

Lemma 2.0.2. *The desired dynamics of the angular axis in (2.28) is locally exponentially stable at the equilibrium point ($\omega_e = 0, q_0 = 0, q = 1$) when the robot is interacting with a frictionless environment, in the sense that $\|q\| \leq \|q(0)\| e^{-\gamma t}, \|\omega_e\| \leq \|\omega_e(0)\| e^{-\gamma t}$, for $\|q(0)\| \in [0, \frac{\sqrt{2}}{2})$ and a positive constant γ. Furthermore the states of the angular axis $\omega_e, q \in \mathcal{L}_1$.*

Proof. we can define a nonnegative function V_ω as follow

$$\begin{aligned} V_\omega &= q^T q + (q_0 - 1)^2 + r^T I_d r && (2.30) \\ &\leq \max\{2, \frac{\lambda_{\max}(I_d)}{2}\}(\|q\|^2 + \|r\|^2) && (2.31) \end{aligned}$$

where $r = \omega_e + K_1 q$. after taking the derivative of (2.30) along (2.28) and (2.27) we can get

$$\begin{aligned} \dot{V}_\omega &= -q^T K_1 q + q^T r + r^T(-Pr - q) && (2.32) \\ &= -q^T K_1 q - r^T P r \end{aligned}$$

then we can have $q, r \in \mathcal{L}_2 \cap \mathcal{L}_\infty, \omega_e, \dot{q}, \dot{r} \in \mathcal{L}_\infty$, then one can utilize Barbalat's lemma to proof $\lim_{t\to\infty} q = \lim_{t\to\infty} r = 0$, this also implies that $\lim_{t\to\infty} \omega_e = 0$, $\lim_{t\to\infty} q_0 = 1$. Inspired by [21], we can also to proof that

$$\dot{V}_\omega \leq -\min\{\lambda_{\min}(K_1), \lambda_{\min}(P)\}(\|q\|^2 + \|r\|^2) \quad (2.33)$$

where $\lambda_{\min}(*)$ and $\lambda_{\max}(*)$ denoting the minimum and maximum eigenvalue of$(*)$. From (2.31) and (2.33), we can have $\dot{V}_\omega \leq -\gamma V_\omega$ where $\gamma = \frac{\min\{\lambda_{\min}(K_1), \lambda_{\min}(P)\}}{\max\{2, \frac{\lambda_{\max}(I_d)}{2}\}}$. Thus we can conclude that the equilibrium point ($q_0 = 1, q = 0, \omega_e = 0$) is exponentially stable. Therefore, we can have $\|q\| \leq \|q(0)\| e^{-\gamma t}, \|\omega_e\| \leq \|\omega_e(0)\| e^{-\gamma t}$. Furthermore, we can bounded $\int_0^\infty \|q\| \, dt, \int_0^\infty \|\omega_e\| \, dt$ as

follow

$$\int_0^\infty \|q\|\, dt \leq \int_0^\infty \|q(0)\|\, e^{-\gamma t} dt < \infty$$

Thus we can have $\omega_e, q \in \mathcal{L}_1$. □

Lemma 2.0.3. *The desired dynamics of the translational axis in (2.20) is Globally exponentially stable at the equilibrium point ($e_v = 0, \dot{e}_v = 0$) when the robot is interacting with a friction-less environment, in the sense that $\|v_{e,z}\| \leq \|v_{e,z}(0)\|\, e^{-\delta t}, \|\dot{v}_{e,z}\| \leq \|\dot{v}_{e,z}(0)\|\, e^{-\delta t}, \|\dot{e}_{v,xy}\| \leq \|\dot{e}_{v,xy}(0)\|\, e^{-\delta t}, \|e_{v,xy}\| \leq \|e_{v,xy}(0)\|\, e^{-\delta t}$ for $e_v(0) \in \mathbb{R}$ and a positive constant δ . Furthermore $v_{e,z}, \dot{v}_{e,z}, \dot{e}_{v,xy}, e_{v,xy} \in \mathcal{L}_1 \cap \mathcal{L}_\infty, f_{e,o}, \tau_e \in \mathcal{L}_\infty$.*

Proof. First we analysis the X,Y axis. The desired dynamic in X,Y axis are as follows

$$\begin{bmatrix} \dot{e}_{v,xy} \\ e_{v,xy} \end{bmatrix} = \begin{bmatrix} -M_d^{-1}B_d & -M_d^{-1}K_d \\ 1 & 0 \end{bmatrix} \begin{bmatrix} e_{v,xy} \\ \int_0^t e_{v,xy} dt \end{bmatrix} \tag{2.34}$$

where $e_{v,xy} = v_{e,xy} - v_{d,xy}, v_{e,xy} = [\ v_{e,x} \quad v_{e,y}\ ]^T, v_{d,xy} = [\ v_{d,x} \quad v_{d,y}\ ]^T$,
$M_{d,xy} = diag[\ m_{d,xy} \quad m_{d,xy}\ ], B_{d,xy} = diag[\ b_{d,xy} \quad b_{d,xy}\ ], K_{d,xy} = diag[\ k_{d,xy} \quad k_{d,xy}\ ]$. It is a linear time invariant system, and the eigenvalues of the system matrix are $\frac{b_{d,xy} \pm \sqrt{b_{d,xy}^2 - 4k_{d,xy}m_{d,xy}}}{2m_{d,xy}}$, since $k_{d,xy}, m_{d,xy}$ are positive, then all the eigenvalue has a negative real part, thus we can conclude that the X,Y axis are exponential stable at the equilibrium point ($e_{v,xy} = 0, \dot{e}_{v,xy} = 0$).

As for the Z axis, since we are assuming there is no friction on the environment, then we can simplify (2.10) as $f_{e,o} = k_e A(x_n - x_o)$, then the desired dynamics are as follow

$$\dot{v}_{e,z} = \frac{1}{m_{d,z}}(-b_{d,z}v_{e,z} + A^T R_o^e f_{e,o} - f_{d,z}) \tag{2.35}$$

$$\dot{f}_{e,o} = -K_e R_e^o v_e \tag{2.36}$$

where $A = [\ 0 \quad 0 \quad 1\ ]^T$. To facilitate the analysis, we can substitute (2.35) and (2.36) into the derivative of (2.35) to derive the dynamics of Z axis in a second order form as follow

$$\ddot{v}_{e,z} = -\frac{b_{dz}}{m_{dz}}\dot{v}_{e,z} - k_e v_{e,z} + G_1 \tag{2.37}$$

$$\begin{aligned} G_1 \;=\; & -k_e A^T H^T v_e - k_e A^T H A v_{e,z} - k_e A^T H A A^T H^T v_e \\ & -A^T [\omega_e]_\times H A \frac{m_{dz}\dot{v}_{e,z} + b_{dz} v_{e,z} + f_{dz}}{A^T R_o^e A} \end{aligned} \tag{2.38}$$

the dynamics system as shown in (2.37) is a perturbed system, the nominal system can be written as follow

$$\ddot{v}_{e,z} = -\frac{b_{dz}}{m_{dz}}\dot{v}_{e,z} - k_e v_{e,z} \tag{2.39}$$

It is a second order linear time invariant system, can also be re-written in states space form as follow

$$\begin{bmatrix} \ddot{v}_{e,z} \\ \dot{v}_{e,z} \\ -\beta e^{-\beta t} \end{bmatrix} = \begin{bmatrix} -\frac{b_{dz}}{m_{dz}} & -k_e & 0 \\ 1 & 0 & 0 \\ 0 & 0 & -\beta \end{bmatrix} \begin{bmatrix} \dot{v}_{e,z} \\ v_{e,z} \\ e^{-\beta t} \end{bmatrix} \tag{2.40}$$

Then we can define a positive definite function V

$$V = \frac{1}{2} x^T P x \tag{2.41}$$

where $x = [\ \dot{v}_{e,z} \quad v_{e,z} \quad e^{-\beta t}\ ]^T$, $P = \begin{bmatrix} m_{dz} & \epsilon m_{dz} & 0 \\ \epsilon m_{dz} & k_e & 0 \\ 0 & 0 & k \end{bmatrix}$, ϵ is a small positive constant. Then

we can have

$$\begin{aligned} \dot{V}_0 &= -x^T Q x \\ &\leq -\lambda_{min}(Q) \|x\|^2 \end{aligned} \tag{2.42}$$

where $Q = \begin{bmatrix} b_{dz} - \epsilon m_{dz} & \frac{1}{2}\epsilon b_{dz} & 0 \\ \frac{1}{2}\epsilon b_{dz} & \epsilon k_e & 0 \\ 0 & 0 & \beta^2 \end{bmatrix}$, when ϵ is sufficient small, then $\dot{V}_0$ will be negative definite, therefor we can conclude the nominal system is exponential stable at the equilibrium point ($\dot{v}_{e,z} = 0, v_{e,z} = 0$). After extensive algebraic manipulation ( ) the perturbation can be linear growth bounded by the states as follow

$$G_1 \leq \max(\gamma_1, \gamma_2, \gamma_3) \|x\|$$

Based on the perturbed system analysis in [22], we can calculate the derivative of V along the trajectories of the perturbed system in (2.37)

$$\begin{aligned} \dot{V} &= \dot{V}_0 + \frac{1}{2} x^T P G + \frac{1}{2} G_1^T P x \\ &\leq -[\lambda_{min}(Q) - \|P\| \max(\gamma_1, \gamma_2, \gamma_3)] \|x\|^2 \end{aligned} \tag{2.43}$$

the $\dot{V}$ will be negative definite for $\lambda_{min}(Q) > \|P\| \max(\gamma_1, \gamma_2, \gamma_3)$. We also have

$$\begin{aligned} \dot{V} &\leq -[\lambda_{min}(Q) - \|P\| \max(\gamma_1, \gamma_2, \gamma_3)] \|x\|^2 \\ &\leq \delta V \end{aligned} \tag{2.44}$$

where δ is a positive constant. Then we can have the states of the Z axis is exponential stable at the equilibrium point($x = 0$). Then we have $\|x\| \leq \|x(0)\| e^{-\delta t}, \|v_{e,z}\| \leq \|v_{e,z}(0)\| e^{-\delta t}, \|\dot{v}_{e,z}\| \leq$

$\|\dot{v}_{e,z}(0)\|\, e^{-\delta t}, \delta = \frac{\lambda_{min}(Q)}{\|P\|} - \max(\gamma_1, \gamma_2, \gamma_3)$. With the same process in the proof of Lemma 2.0.2, we can have $v_{e,z}, \dot{v}_{e,z}, \dot{e}_{xy}, e_{xy} \in \mathcal{L}_1 \cap \mathcal{L}_\infty$, and according to (2.35), we can have $f_{e,o} \in \mathcal{L}_\infty$. We also have $\lim_{t\to\infty} v_{e,z} = \lim_{t\to\infty} \dot{v}_{e,z} = 0$,and $\lim_{t\to\infty} f_{e,e} = f_{d,z}$, and since $\tau_e = f_{e,e} \times r_{off} \leq \|f_{e,e}\|\, \|r_{off}\| <= \sup\{\|f_{e,e}\|\}\, \|r_{off}\| < \infty$, we can have $\tau_e \in \mathcal{L}_\infty$. □

From the Lemma 2.0.1 we can have the closed loop dynamics achieves the desired dynamics in (2.20), (2.28). Such that we can project the desired impedance on the frictionless environment. Based on Lemma 2.0.2, since the quaternion which represents the misalignment converge to zero, then we can have that the robot end-effector align with the frictionless environment. Furthermore, according to Lemma 2.0.2 we can have the end-effector can control the end-effector velocity on the environment tangential axes, also apply the desired amount of force in the environment normal direction.

From the above Lemmas, we can also have the main passivity result for the proposed controller in the following theorem:

Theorem 2.0.4. *The proposed control law can ensure the work done by the robot to the frictionless environment(human) is limited,* $W = \int_0^\infty (-F_{env})^T v_e dt \leq c < \infty$.

Proof. (1) Before reach the desired dynamics

Since the sliding mode control has a finite time convergence. It will drive the system dynamics to the desired dynamics in finite time $t1$. After $t1$, S and $\dot{S}$ will converge to 0. So the work done by the robot from $t = 0$ to $t = t_1$ is as follow

$$\begin{aligned} W_b &= \int_0^{t1} (-F_{env})^T v_e dt \\ &= -\int_0^{t1} f_{e,xy}^T v_{xy} dt - \int_0^{t1} f_{e,z}^T v_{e,z} dt - \int_0^{t1} \tau_e^T \omega_e dt \end{aligned} \tag{2.45}$$

Based on the stability analysis of the sliding mode controller, we can have $S \in \mathcal{L}_1 \cap \mathcal{L}_\infty, \dot{S} \in \mathcal{L}_\infty$ in $[0, \infty]$, then we can also have $S, \dot{S} \in \mathcal{L}_\infty$ in $[0, t_1]$. According to (2.15), (2.14) and (2.21),we can have $J^+ R\dot{e}_{v,e}, J^+ a_x \in \mathcal{L}_\infty$ in $[0, t_1]$. Assume the manipulator never runs into singularity, then we can have $J^+ \in \mathcal{L}_\infty$, since R is also bounded, then we can have $e_v, e_f, v_e, F_{env} \in \mathcal{L}_\infty$.Therefore we can have the work done by the end-effector to the environment is upper bounded as follow

$$\begin{aligned} W_b &= \int_0^{t1} (-F_{env})^T v_e dt && (2.46) \\ &\leq \sup\{\|v_e\|\} \sup\{\|F_{env}\|\} t_1 \\ &\leq c_b && (2.47) \end{aligned}$$

(2) After reach the Desired Dynamics

The work done by the robot to the environment is denoted by $W_a(t)$, and given by

$$\begin{aligned} W_a &= \int_{t1}^{t} (-F_{env})^T v_e dt && (2.48) \\ &= -\int_{t1}^{t} f_{e,xy}^T v_{e,xy} dt - \int_{t1}^{t} f_{e,z}^T v_{e,z} dt - \int_{t1}^{t} \tau_{e,e}^T \omega_e dt \\ &\leq \int_{t1}^{t} \|f_{e,xy}\| \, \|v_{e,xy}\| \, dt + \int_{t1}^{t} \|f_{e,z}\| \, \|v_{e,z}\| \, dt \\ &\quad + \int_{t1}^{t} \|\tau_e\| \, \|\omega_e\| \, dt \end{aligned}$$

since we have $f_{e,o}, v_{e,xy}, \tau_e \in \mathcal{L}_\infty$, Then we can bounded (2.48) as follow

$$\begin{aligned} W_a &\leq \sup\{\|v_{xy}\|\} \int_{t1}^{t} \|f_{e,xy}\| \, dt && (2.49) \\ &\quad + \sup\{\|f_{e,z}\|\} \int_{t1}^{t} \|v_{e,z}\| \, dt + \sup\{\|\tau_e\|\} \int_{t1}^{t} \|\omega_e\| \, dt \end{aligned}$$

for the first term, we can bound the $\int_{t1}^{t} \|f_{e,xy}\|$ as follow

$$\begin{aligned} & \int_{t1}^{t} \|f_{e,xy}\| \, dt \\ = & \int_{t1}^{t} \left\|A_{xy}^{T} R_{o}^{e} f_{e,o}\right\| dt \\ \leq & \int_{t1}^{t} \left\|A_{xy}^{T} R_{o}^{e} A\right\| \|f_{e,o}\| \, dt \\ \leq & \sup\{\|f_{e,o}\|\} \int_{t1}^{t} \left\|A_{xy}^{T} R_{o}^{e} A\right\| dt \end{aligned} \tag{2.50}$$

where $A_{xy} = [\ 1 \quad 1 \quad 0\ ]^{T}$.Since $R_{o}^{e} = I - 2q_{m}^{T} q_{m} I + 2q_{m} q_{m}^{T} - 2q_{m0}[q_{m}]_{\times}$, then we can have $A_{xy}^{T} R_{o}^{e} A = 2q_{m0}(q_{m1} - q_{m2})$, $q_{m} = [\ q_{m1} \quad q_{m2} \quad 0\ ]$, then we can bounded $\int_{t0}^{t} \|f_{e,xy}\|$ as follow

$$\begin{aligned} & \sup\{\|f_{e,o}\|\} \int_{t1}^{t} \left\|A_{xy}^{T} R_{o}^{e} A\right\| dt \\ = & \sup\{\|f_{e,o}\|\} \int_{t1}^{t} \|2q_{m0}(q_{m1} - q_{m2})\| \, dt \\ \leq & 2 \sup\{\|f_{e,o}\|\} \int_{t1}^{t} (\|q_{m1}\| + \|q_{m2}\|) dt \\ \leq & 2 \sup\{\|f_{e,o}\|\} \int_{t1}^{t} \|q_{m}\| \, dt \end{aligned} \tag{2.51}$$

Since $q_{m}, \nu_{e,z}, \omega_{e}$ are exponential stable, then we can proof $q, \nu_{e,z}, \omega_{e} \in \mathcal{L}_{1}$, then we can have $\int_{t1}^{t} |q| \, dt \leq c_{2} < \infty$, $\int_{t1}^{t} |\nu_{e,z}| \, dt \leq c_{3} < \infty$, $\int_{t1}^{t} |\omega_{e}| \, dt \leq c_{4} < \infty$, where c_{2}, c_{3}, c_{4} are positive constant. Then we can bounded W_{a} as follow

$$\begin{aligned} W_{a} \leq & 2 \sup\{\|\nu_{e,xy}\|\} \sup\{\|f_{e,o}\|\} c_{2} \\ & + \sup\{\|f_{e,z}\|\} c_{3} + \sup\{\|\tau_{e,e}\|\} c_{4} \\ \leq & c_{total} \end{aligned} \tag{2.52}$$

Therefore, we can conclude that the work done by the robot end-effector $W = W_{a} + W_{b} < \infty$

. □

Simulation Results

During the simulation, 0s-5s is the initial alignment phase, the command velocity in X and Y direction are both $0cm/s$. From 5s-20s and 20s-35s, we command the desired velocity for $\pm 1.5cm/s$ along the end-effector Y direction. And from 35s-40s, we also command $0cm/s$ velocity on the tangential direction of end-effector.

From the Figures 2.4-2.8, we can see that the proposed controller can regulated the force error in end-effector Z direction to zero after the initial alignment process. The end-effector velocity along the tangential directions also tracks the desired velocity within a near 0 tracking error. As for the alignment, the norm of the quaternion $\|q\|$ and the misalignment angle decrease to 0. We also defined another value to evaluate the alignment, the equivalent level $r_{tan} = \sqrt{F_z^2/(\tau_x^2 + \tau_y^2)}$ which represents the length of the projection of level arm r_e in end-effector x,y plane, when the end-effector is aligned with the environment, r_{tan} also converges to zero. In Figure 2.8, we can also see that the r_{tan} decreased to 0 as the misalignment angle converge to 0.

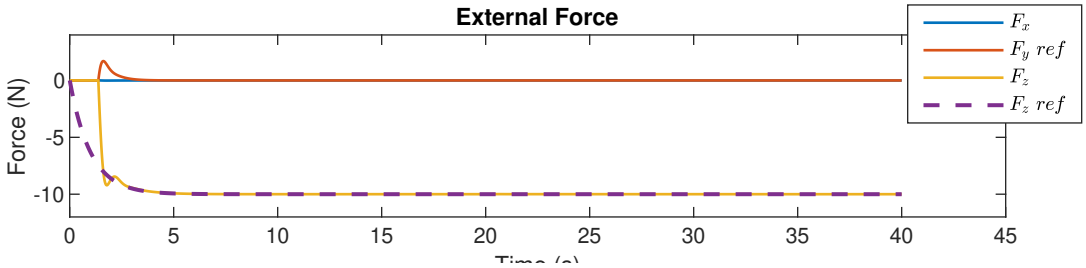

Figure 2.4: External force profile. The top plot is the result of proposed robust controller. The bottom plot is the result of the hybird controller without SMC.

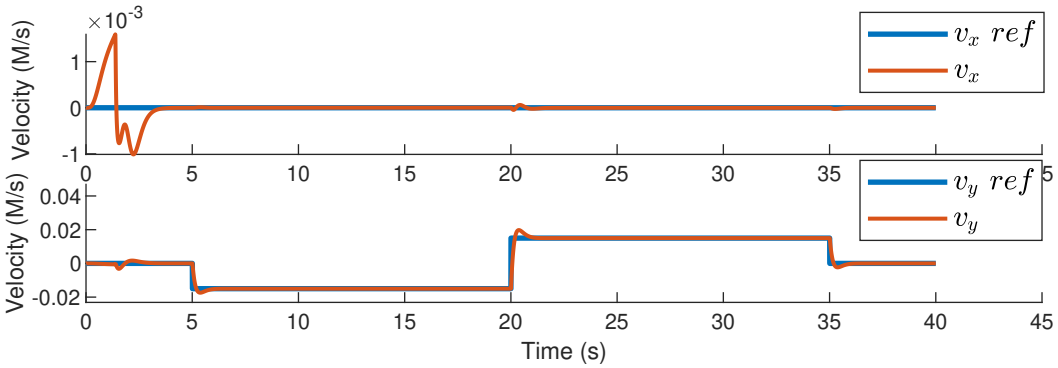

Figure 2.5: Velcity tracking profile.

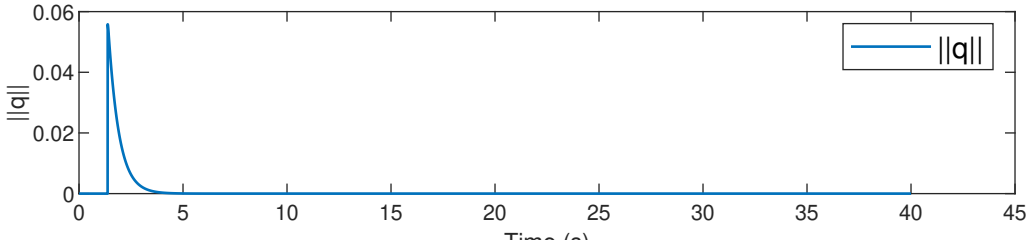

Figure 2.6: Quaternion tracking profile.

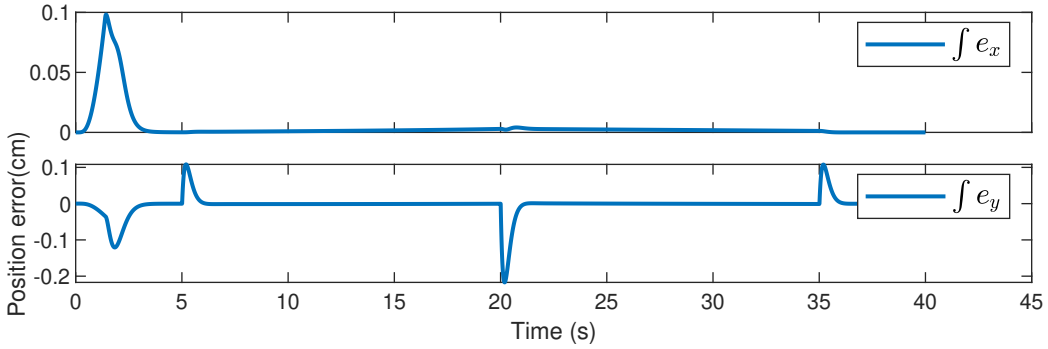

Figure 2.7: Position tracking profile.

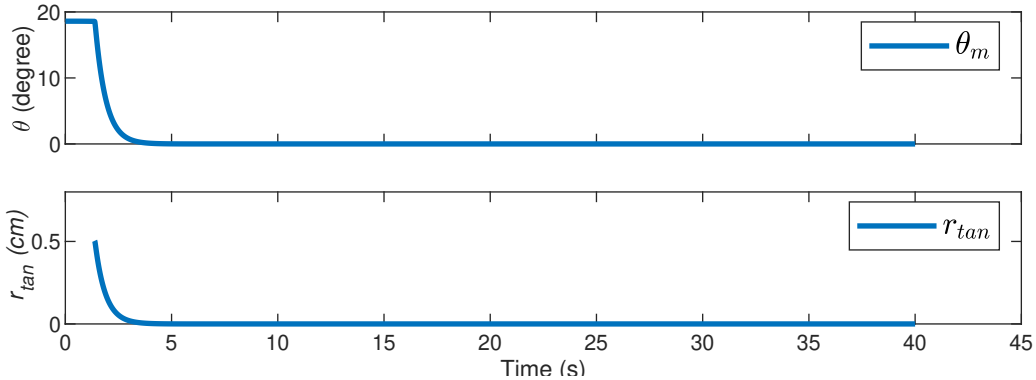

Figure 2.8: Misalignment evaluation. The top plot is the misalign angle between the end-effector z diretion and norm of the contact surface. The bottom plot is the equivalent lever in end-effector tangential direction.

Control Design and Stability Analysis for Frictional Environment

Control Design

In above section, we can see that the proposed controller is safe and performance good with the frictionless environment. In this section we will introduce the controller for the frictional environment which is closer to the real world. For the case with friction, we can design the sliding mode control and torque input the same with (2), but if we don't compensate the friction, even though the equilibrium of the angular axis remains the same ($q_0 = 1, q = 0, \omega_e = 0$), but the quaternion is now representing the rotation between r_e and $f_{e,e}$, then the equilibrium represents $r_e // f_{e,e}$. And the $f_{e,e} = f_o + f_f$ which is the net force of the friction force f_f and the normal force f_o, so the angle between the environment normal and the r_e is $\theta_o = \arctan(\frac{f_f}{f_o})$, and according to the geometry, we can have the misalignment angle θ_m between the end-effector and the environment normal

$$\|r_{off}\| \sin(\theta_m) = \|r_e\| \sin(\theta_o) \tag{2.53}$$

$$\theta_m = \arcsin(\frac{\|r_e\|}{\|r_{off}\|} \sin(\arctan(\frac{f_f}{f_o}))) \tag{2.54}$$

which is related to the surface friction and environment normal force. The relative position between the end-effector and environment is also shown in Figure 2.9.

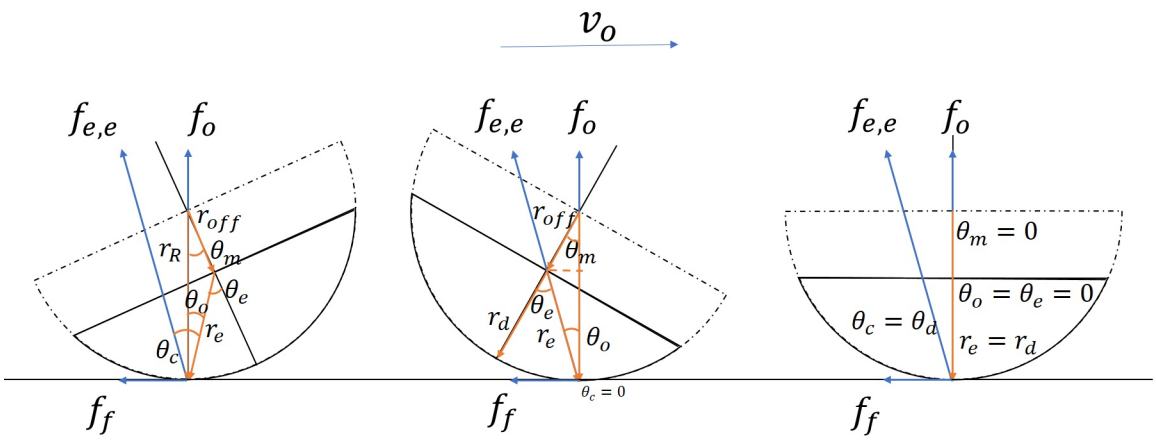

Figure 2.9: Geometry of the end-tool. Left plot is the general misalign case for the environment with friction. Middle plot is the equilibrium of the controller in last section is applied in the frictional environment. The right plot is the desired equilibrium for the frilctional environment.

To align the end-effector with the environment, we have to compensate the effect from the friction. We designed a desired torque $\tau_d \triangleq r_d \times f_{e,e}$ and extract the desired quaternion $q_d(q_d, q_{d0})$ which representing the rotation between the desired level arm $r_d \triangleq (\|r_R\| - \|r_{off}\|)\hat{z}_e$ and environment force $f_{e,e}$. Similar with the case without friction in (2), since we don't know the value of $\|r_e\|$, so we normalized it with $\|r_M\|$ as well. Then the definition of $q(q, q_0)$ and $q_d(q_d, q_{d0})$ are as follow

$$q_0 = \cos(\frac{\acute{\theta}_c}{2}), q = \sin(\frac{\acute{\theta}_c}{2})n_e \tag{2.55}$$

$$q_{d0} = \cos(\frac{\acute{\theta}_d}{2}), q_d = \sin(\frac{\acute{\theta}_d}{2})n_d \tag{2.56}$$

where $n_e = \frac{\tau_e}{\|\tau_e\|}, \sin(\acute{\theta}_c) \triangleq k_1 \sin(\theta_c) = \frac{\|\tau_e\|}{\|r_M\|\|f_{e,e}\|}, k_1 = \frac{\|r_e\|}{\|r_M\|}, n_d = \frac{\tau_d}{\|\tau_d\|}, \sin(\acute{\theta}_d) \triangleq k_2 \sin(\theta_d) = \frac{\|\tau_d\|}{\|r_M\|\|f_{e,e}\|}, k_2 \triangleq \frac{\|r_d\|}{\|r_M\|}$, and $k_2 < 1$ is a constant, $k_2 \leq k_1 \leq 1$ is varying respect to θ_c. Then we

define the quaternion error $e(e, e_0)$ based on q and q_d

$$\begin{aligned} e &= q_d^{-1} \circ q \\ e_0 &= q_0 q_{0d} + q^T q_d \\ e &= q_{0d} q - q_0 q_d + [q]_\times q_d \end{aligned} \tag{2.57}$$

And the dynamics of the quaternion are as follows

$$\begin{aligned} \dot{e}_0 &= -\tfrac{1}{2}\omega_e^T e \\ \dot{e} &= \tfrac{1}{2}(e_0 \omega_e + e \times \omega_e) \end{aligned} \tag{2.58}$$

Then the desired dynamics of the rotation axis are as follow

$$I_d \dot{\omega}_e + B_{d,\omega f}\omega_e = \tau_{a,f} \tag{2.59}$$

where $r = \omega_e + K_1 e$, $B_{d,\omega f} = \frac{1}{2}(e_0 I_d K_1 + 4P + [e]_\times)$, $\tau_{a,f} = -Pe - e$. Then we have the auxiliary control term $a_{x,\omega}$ as follow

$$a_{x,\omega} = R I_d^{-1}[\tau_{a,f} - B_{d,\omega f}\omega_e] \tag{2.60}$$

Stability Analysis

Lemma 2.0.5. *The desired dynamics of the angular axis in (2.59) is locally exponentially stable at the equilibrium point ($\omega_e = 0, e = 0, e_0 = 1$) when the robot is interacting with a frictional environment, in the sense that $\|e\| \leq \|e(0)\| e^{-\gamma t}, \|\omega_e\| \leq \|\omega_e(0)\| e^{-\gamma t}$, for $\|e(0)\| \in [0, \frac{\sqrt{2}}{2})$ and a positive constant γ. Furthermore the states of the angular axis $\omega_e, e \in \mathcal{L}_1$.*

Proof. For the environment with friction, our sliding mode control remains the same, but the de-

sired dynamics in angular axis are different. Based on the desired dynamics in (2.59) and the dynamics of quaternion error in (2.58) we can define a positive function similar with (2.30) as follow

$$V_\omega = e^T e + (e_0 - 1)^2 + r^T I_d r \tag{2.61}$$

where $r = \omega_e + K_1 e$, by taking the derivative of (2.61), we can have

$$\dot{V}_\omega = -e^T K_1 e - r^T P r$$

With the similar process in (2), we can also have the angular axis is still exponential stable at the equilibrium point($e_0 = 1, e = 0, \omega_e = 0$). Therefore, we can have $\|e\| \leq \|e(0)\| e^{-\gamma t}, \|\omega_e\| \leq \|\omega_e(0)\| e^{-\gamma t}$. Furthermore, we can bounded $\int_0^\infty \|e\| dt, \int_0^\infty \|\omega_e\| dt$ as follow

$$\int_0^\infty \|e\| dt \leq \int_0^\infty \|e(0)\| e^{-\gamma t} dt < \infty$$

Thus we can have $\omega_e, e \in \mathcal{L}_1$. □

Lemma 2.0.6. *The desired dynamics of the translational axis in (2.20) is globally exponentially stable at the equilibrium point ($e_{v,e} = 0, \dot{e}_{v,e} = 0$) when the robot is interacting with a frictional environment, in the sense that $\|v_{e,z}\| \leq \|v_{e,z}(0)\| e^{-\delta t}, \|\dot{v}_{e,z}\| \leq \|\dot{v}_{e,z}(0)\| e^{-\delta t}, \|\dot{e}_{v,xy}\| \leq \|\dot{e}_{v,xy}(0)\| e^{-\delta t}, \|e_{v,xy}\| \leq \|e_{v,xy}(0)\| e^{-\delta t}$ for $e_{v,e}(0) \in \mathbb{R}$ and a positive constant δ. Furthermore $v_{e,z}, \dot{v}_{e,z}, \dot{e}_{xy}, e_{xy} \in \mathcal{L}_1 \cap \mathcal{L}_\infty, f_{e,o}, \tau_e \in \mathcal{L}_\infty$.*

Proof. The analysis for rotational axis and X,Y axis remains the same in (2). But the model of the environmental force has the damping term as shown in (2.10). Then we have the derivative of $f_{e,o}$

as follow

$$\begin{aligned} \dot{f}_{e,o} &= -k_e A \dot{x}_o - B_e \dot{v}_o \\ &= -K_e R_e^o v_e - B_e (R_e^o \dot{v}_e + R_e^o [\omega_e]_\times v_e) \end{aligned} \tag{2.62}$$

then we can re-write the dynamics of Z axis in second order form as follows

$$\begin{aligned} m_{dz} \ddot{v}_{e,z} &= -b_{dz} \dot{v}_{e,z} + A^T \dot{R}_o^e f_{e,o} + A^T R_o^e \dot{f}_{e,o} \\ &= -b_{dz} \dot{v}_{e,z} - k_e v_{e,z} + G_1 + G2 \end{aligned} \tag{2.63}$$

where

$$G_2 = -A^T R_o^e [B_e (R_e^o \dot{v}_e + R_e^o [\omega_e]_\times v_e)]$$

The new dynamics of Z axis (2.63) shares the same nominal system with non-friction case. After extensive algebraic manipulation ( ), we can bounded H_2 exponentially. Since H_2, ω_e are exponentially bounded, $v_{e,xy} \in \mathcal{L}_\infty$, with the similar process in ( ), we can bounded the perturbation term $G + G_2$ as follows

$$\begin{aligned} \|G_1 + G_2\| &\leq \gamma_4 \|\dot{v}_{e,z}\| + \gamma_5 \|v_{e,z}\| + \gamma_6 e^{-\beta t} \\ &\leq \max(\gamma_4, \gamma_5, \gamma_6) \|x\| \end{aligned} \tag{2.64}$$

where $\gamma_4, \gamma_5, \gamma_6$ are positive constant. Then we can construct a similar positive definite function as (2.41)

$$V_f = \frac{1}{2} x^T P x \tag{2.65}$$

which has the same definition of x, P with (2.41). Then we can have the derivative of (2.65)

$$\begin{aligned} \dot{V}_f &= \dot{V}_0 + \frac{1}{2}x^T P(G_1 + G_2) + \frac{1}{2}(G_1 + G_2)^T P x \\ &\leq -\lambda_{min}(Q)\,\|x\|^2 + \|x\|\,\|G_1 + G_2\|\,\|P\| \\ &\leq -[\lambda_{min}(Q) - \max(\gamma_4, \gamma_5, \gamma_6)]\,\|x\|^2 \end{aligned} \tag{2.66}$$

the $\dot{V}_f$ will be negative definite for $\lambda_{min}(Q) > \|P\| \max(\gamma_4, \gamma_5, \gamma_6))$. We also have

$$\begin{aligned} \dot{V}_f &\leq -[\lambda_{min}(Q) - \|P\| \max(\gamma_4, \gamma_5, \gamma_6)]\,\|x\|^2 \\ &\leq \delta_2 V_f \end{aligned} \tag{2.67}$$

where δ_2 is a positive constant. Such that, we have the $v_{e,z} = 0, \dot{v}_{e,z} = 0$ are also exponential stable. With the same analysis in the proof of Lemma 2.0.3 we can also have $f_{e,o}, \tau_e \in \mathcal{L}_\infty$. □

Similar with Remark 2. From the lemma 2.0.1 we can have the closed loop dynamics achieves the desired dynamics in (2.20), (2.59). Such that we can project the desired impedance on the frictional environment. Based on Lemma 2.0.5 and 2.0.6, we can have that the robot end-effector will align with the frictionless environment and control the end-effector velocity on the environment tangential axes, also apply the desired amount of force in the environment normal direction.

Then is the passivity result of the manipulator:

Theorem 2.0.7. *The proposed control law can ensure the extra work done by the robot to the frictional environment(human) is limited.*

Proof. Because of the environment surface is a resistive environment, so any relative motion in the surface will generate a certain mount of energy. In this case, the passivity in the end-effector X,Y axis is not valid. But we can still define a baseline for the work done by the end-effector to the

environment in X,Y axis $W_d \triangleq \int P_d$. $P_d \triangleq -f_f^T v_{d,xy}$ is the power of the friction force and desired velocity along the environment. Therefore W_d, P_d is the minimum work and power for approach the desired movement along the environment.

$$
\begin{aligned}
f_f &= -B_e v_{d,xy} && (2.68)\\
W_d &\triangleq \int_0^t P_d dt && (2.69)\\
&= b_e \int_0^t v_{d,xy}^T v_{d,xy} dt
\end{aligned}
$$

We can also have the actual work done by the end-effector to the environment in X,Y axis as follow

$$
\begin{aligned}
W_{xy} &= \int_0^t -f_{e,xy}^T v_{e,xy} dt && (2.70)\\
&= \int_0^t (B_e v_e)^T A_{xy} v_e dt + \int_0^t (v_e^T B_e^T H_2^T A_{xy} v_e \\
&\quad + v_e^T H_2 B_e^T A_{xy} v_e + v_e^T H_2 B_e^T H_2^T A_{xy} v_e) \\
&\quad - \int_0^t {f_{o,z}}^T R_o^e A_{xy}^T A_{xy} v_e dt \\
&\leq W_d + b_e \sup\{\|v_{e,xy}\|^2\} \int_0^t (2\|H_2\| + \|H_2\|^2) dt \\
&\quad + \sup\{\|f_{e,o}\|\} \sup\{\|v_{e,xy}\|\} \int_0^t \left\| A^T R_o^e A_{xy} \right\| dt \\
&\leq W_d + b_e \sup\{\|v_{e,xy}\|^2\} \int_0^t (2\|H_2\| + \|H_2\|^2) dt \\
&\quad + \sup\{\|f_{e,o}\|\} \sup\{\|v_{e,xy}\|\} \int_{t0}^t \|e\| dt
\end{aligned}
$$

Since we have H_2 and e are exponentially stable and $H_2, e \in \mathcal{L}_1$, then we can rearrange (2.70)

bounded the difference between W_{xy} and W_d as follow

$$\begin{aligned} W_{xy} - W_d &\leq b_e \sup\{\|v_{e,xy}\|^2\} \int_0^t (2\|H_2\| + \|H_2\|^2) dt \\ &\quad + \sup\{\|f_{e,o}\|\} \sup\{\|v_{e,xy}\|\} \int_{t0}^t \|e\| \, dt \\ &\leq c_{xy} \end{aligned} \tag{2.71}$$

where c_{xy} is a positive value. Then we can conclude that the extra work done by the robot compared with the desired minimum work is bounded. The work done by the robot to the environment in the rest of axis is denoted by $W_r(t)$, and given by

$$\begin{aligned} W_r &= \int_{t1}^t f_{e,z}^T v_{e,z} dt - \int_{t1}^t \tau_e^T \omega_e dt \\ &\leq \int_{t1}^t \|f_{e,z}\| \|v_{e,z}\| \, dt + \int_{t1}^t \|\tau_e\| \|\omega_e\| \, dt \end{aligned} \tag{2.72}$$

where W_{xy} is the work done by the end-effector on X,Y axis. since we have $f_{e,o}, v_{xy}, \tau_{e,e} \in \mathcal{L}_\infty$, Then we can bounded (2.72) as follow

$$W_r \leq \sup\{\|f_{e,z}\|\} \int_{t1}^t \|v_{e,z}\| \, dt + \sup\{\|\tau_e\|\} \int_{t1}^t \|\omega_e\| \, dt \tag{2.73}$$

Since $v_{e,z}, \omega_e$ are exponential stable, then we can proof $v_{e,z}, \omega_e \in \mathcal{L}_1$, then we can have $\int_{t1}^t \|v_{e,z}\| \, dt \leq c_3 < \infty$, $\int_{t1}^t \|\omega_e\| \, dt \leq c_4 < \infty$, where c_3, c_4 are positive constant. Then we can bounded W as follow

$$\begin{aligned} W_r &\leq \sup\{\|f_{e,z}\|\} c_3 + \sup\{\|\tau_e\|\} c_4 \\ &\leq c_r \end{aligned} \tag{2.74}$$

From (2.71) and (2.74), we can conclude that the proposed controller will only apply a limit amount

of work to the environment with friction. So the proposed controller is safe for the environment with friction as well. □

Simulation Results

In order to closely mirror experimental reality, we add joint friction, measurement noise, imperfect gravity compensation, and imperfect robot inertial matrix to the simulation studies. The joint friction model utilized is as follows

$$\begin{aligned} \tau_f &= F_c sng(q_i)[1 - \exp(\frac{-\dot{q}_i^2}{v_s})] \\ &\quad + F_{si} sng(\dot{q}_i) \exp(\frac{-\dot{q}_i^2}{v_s}) + F_v \dot{q}_i \end{aligned} \tag{2.75}$$

where F_c, F_s, F_v are the Coulomb, static, and viscous friction coefficients while v_s is the Stribeck parameter. We also add measurement noise which follows a normal distribution with $\mu = -0.0001, \sigma = 0.0315$. We assume there is a 3% imperfect gravity compensation in the simulation. As for the imperfect robot inertial matrix, we assume there is a constant 20% error of the inertial matrix for the last three joints. We modeled plane surface for the simulation. We also replace the $sign(S)$ function in the sliding mode control with a continues function $\tanh(S)$ for decrease the chattering phenomenon. All the parameters for each joint are listed in Table 2.1.

From Figures 2.10-2.14, we can see the similar performance with the proposed control with frictionless environment. The force error in Z axis is regulated within 0.5N. The force in Y axis is the friction force from the environment surface. And the quaternion error is also regulated within 0.01 which means the relative attitude between the end-effector Z axis and environment normal converges to $q_m (q_m = 0, q_{m0} = 1)$. We can also see the same alignment results from Figure 2.13, the misaligned angle converges to 0. The velocity and position tracking in X,Y axis also

Table 2.1: Simulation parameters

$F_c = diag[\ 0.07 \quad 0.07 \quad 0.07 \quad 0.07 \quad 0.014 \quad 0.014 \quad 0.0035\ ]$
$F_s = diag[\ 0.14 \quad 0.14 \quad 0.14 \quad 0.14 \quad 0.028 \quad 0.028 \quad 0.007\ ]$
$F_v = diag[\ 0.13 \quad 0.13 \quad 0.13 \quad 0.13 \quad 0.026 \quad 0.026 \quad 0.013\ ]$
$v_s = diag[\ 0.01 \quad 0.01 \quad 0.01 \quad 0.01 \quad 0.01 \quad 0.005 \quad 0.005\ ]$
$M_{d,v} = diag[\ 1 \quad 1 \quad 10\ ]$
$I_d = diag[\ 0.3 \quad 0.3 \quad 0.3\ ]$
$B_{d,v} = diag[\ 10 \quad 10 \quad 70\ ]$
$K_d = diag[\ 30 \quad 30 \quad 0 \quad 0 \quad 0 \quad 0\ ]$
$Q = diag[\ 24 \quad 48 \quad 48 \quad 60 \quad 72 \quad 72 \quad 84\ ]$
$P = diag[\ 4 \quad 4 \quad 4\ ]$
$K_1 = diag[\ 10 \quad 10 \quad 10\ ]$
$K_e = diag[\ 0 \quad 0 \quad 506\ ]$
$B_e = diag[\ 100 \quad 100 \quad 0\ ]$

performs as expected, the tracking error is regulated within 0.2 cm. From the Figure 2.14, we can see that the sliding mode control signal will always covers disturbance, therefore converge the system dynamics to the desired dynamics.

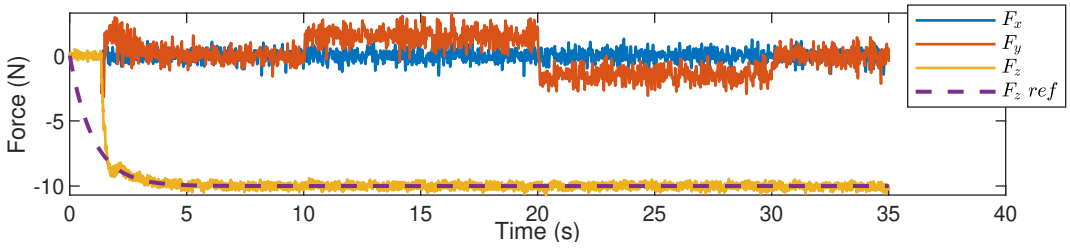

Figure 2.10: Force tracking profile for frictional environment.

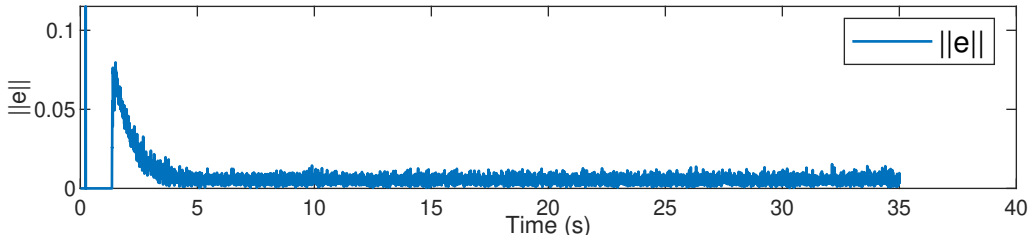

Figure 2.11: Quaternion error tracking profile for frictional environment.

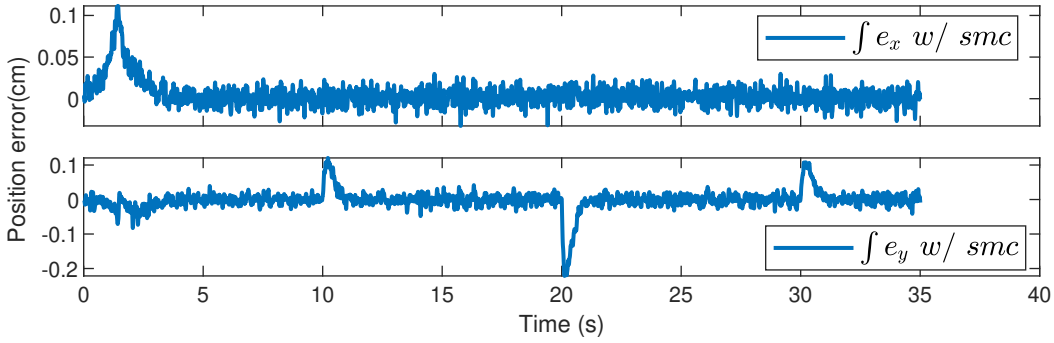

Figure 2.12: Velocity tracking profile for frictional environment.

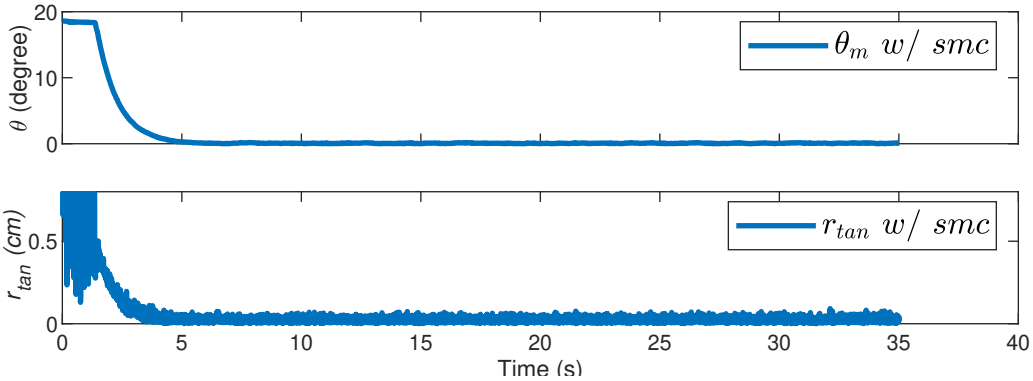

Figure 2.13: Alignment evaluation for frictional environment.

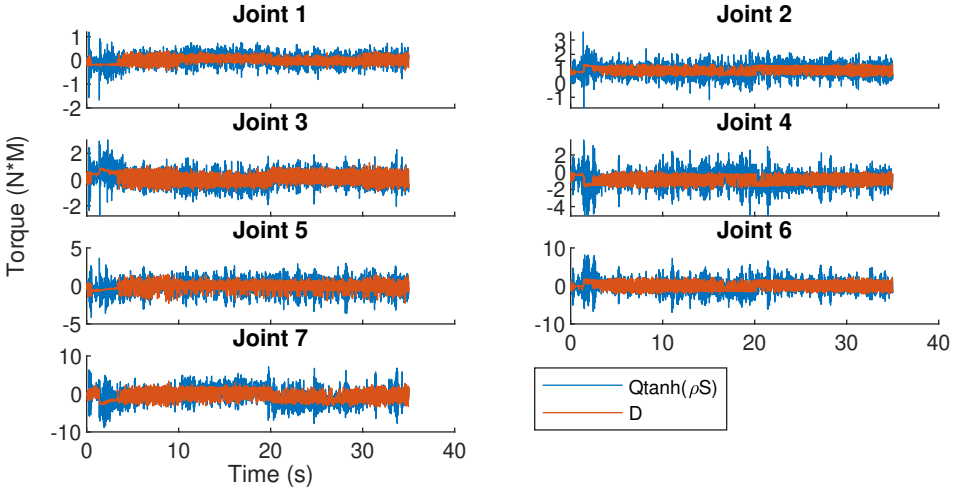

Figure 2.14: SMC performance for frictional environment.

Experimental Results

For the experiment, the Baxter robot from Rethink Robotics was used as the testbed. The ATI Mini45 force/torque sensor was mounted on the wrist of the Baxter to sense the interaction force/-torque. The sensor was covered by a soft rubber to lower the stiffness of the end-tool. As for the signal processing, we utilized an averaging filter with 45-sample window on the 1000Hz Baxter status publish node. In the experiments, we simplified the controller (2.14) and (2.60) as follow

$$a_j = J^+ a_x - KS - Q\tanh(S) \tag{2.76}$$

$$a_{x,\omega} = RI_d^{-1}[-B_{d\omega}\omega_e + e_\tau] \tag{2.77}$$

where $e_\tau \triangleq \tau_e - \tau_d, \tau_d \triangleq r_d \times f_{e,e}, K$ is a constant diagonal matrix, $I_d \triangleq diag\{i_d, i_d, i_d\}$, $B_{d\omega} \triangleq diag\{b_{d,\omega}, b_{d,\omega}, b_{d,\omega}\}$ denote the desired rotational inertia, damping, all elements in the matrices are positive constant. The experiments include 1) align the end effector to a yoga ball, 2) move the end effector along the yoga ball, 3) move the end effector along a mannequin.

In the first alignment experiment, we command $0cm/s$ velocities to the end-effector and $(1 - e^{-0.2*t}) * 10N$ as the desired force in the end-effector Z direction. From Figures 2.15 - 2.19, we can see that the interaction force along the end-effector Z direction was regulated around 10N with $\pm 0.5N$ error. And the position error is less than $0.2cm$ after the end-effector aligned with the surface. The interaction torque also decreases to less than $0.005N \cdot m$, and the equivalent lever finally stays around $0.3mm$, both results represent the end-effector is highly aligned with the yoga ball.

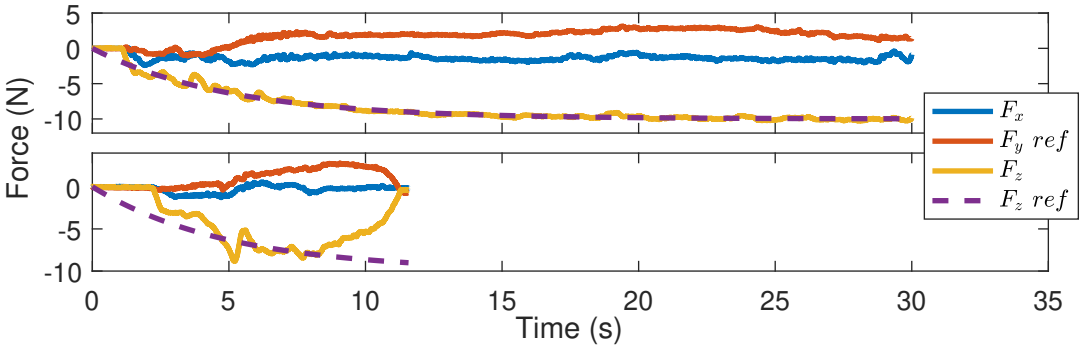

Figure 2.15: External force for ball alignment.

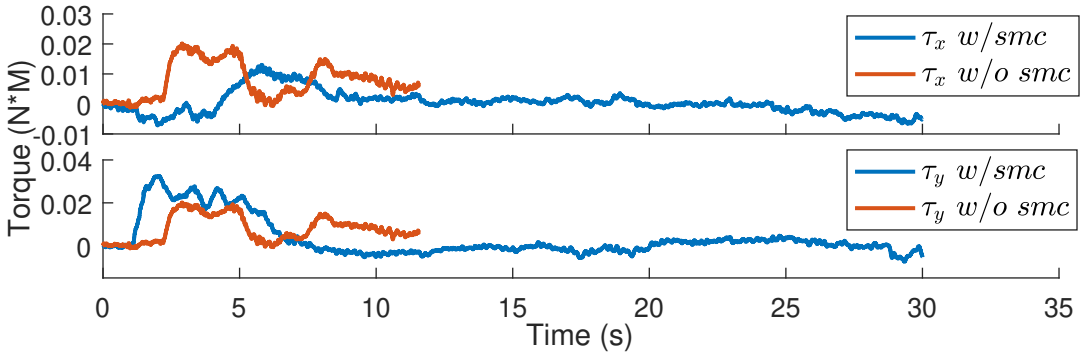

Figure 2.16: External torque for ball alignment.

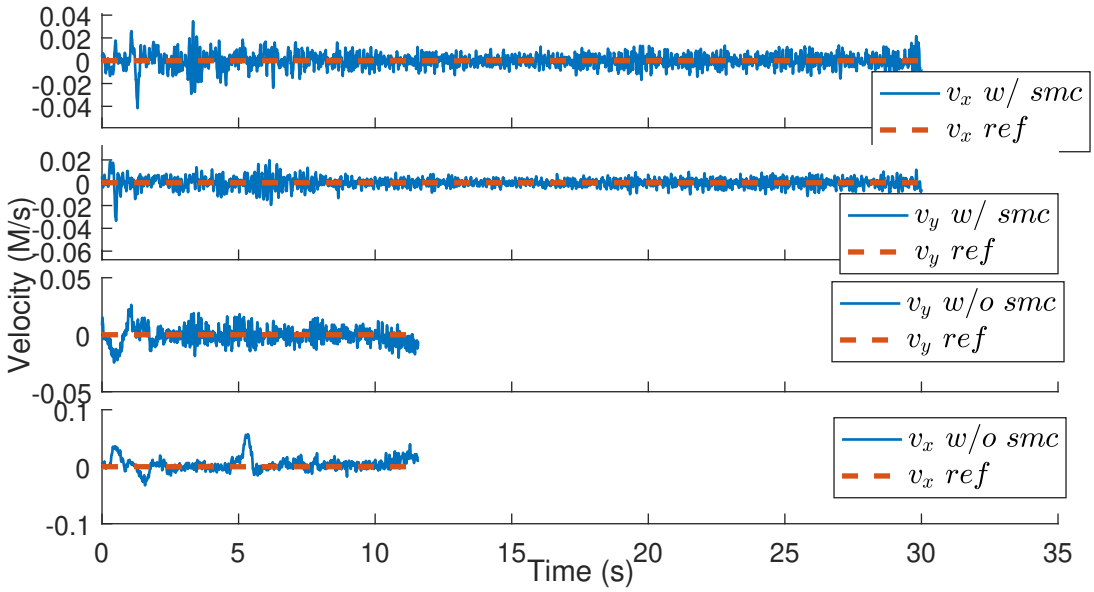

Figure 2.17: Velocity tracking for ball environment alignment experiment.

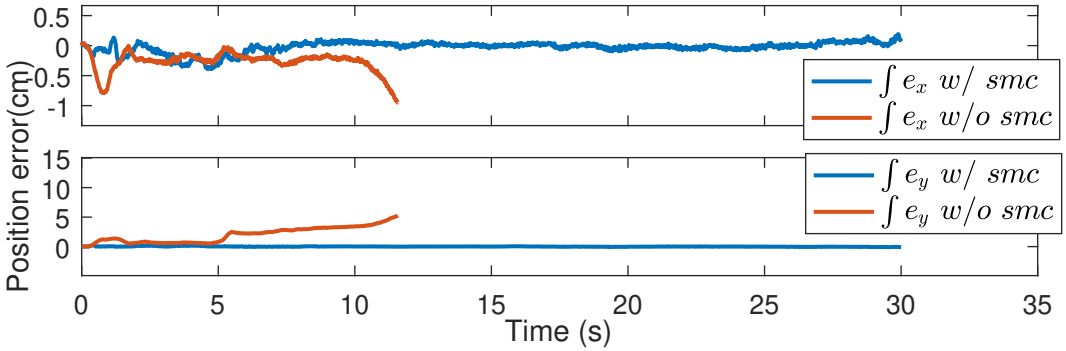

Figure 2.18: Position tracking and error for ball environment alignment experiment.

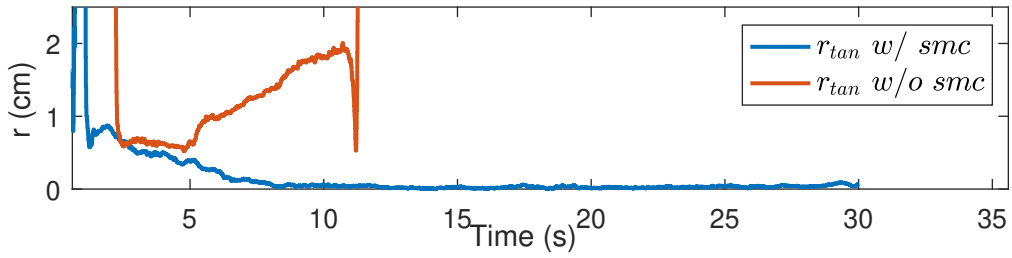

Figure 2.19: Alignment evaluation for ball environment alignment.

In the second experiment, we also command $(1 - e^{-0.2*t}) * 10\text{N}$ as the desired force in the end-effector Z direction and the desire velocity was set to 0 from 0-10s for the initial alignment, $\pm 1.5\text{cm/s}$ along end-effector x direction during the movement. From the Figure 2.20 - 2.24, the force along end-effector Z direction still can regulated around 10N, and also moves on the yoga ball with the desired velocity. And we can notice that the torque error on pitch axis is around $\pm 0.015\text{N} \cdot \text{m}$. As we discussed in simulation part, this torque error drives the end-effector to perform a constant angular velocity to align with the surface during the movement.

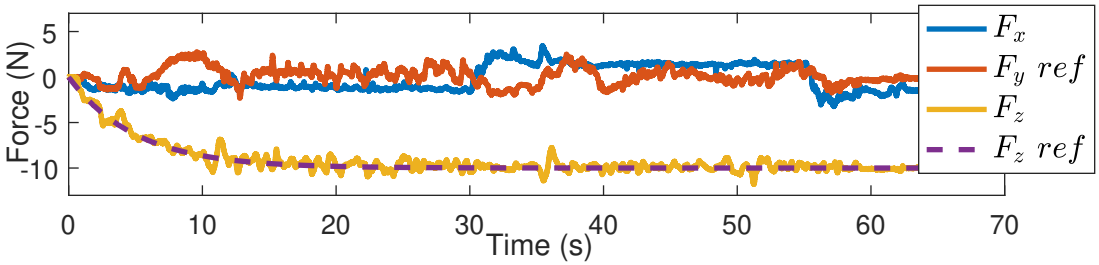

Figure 2.20: External force for moving on ball environment.

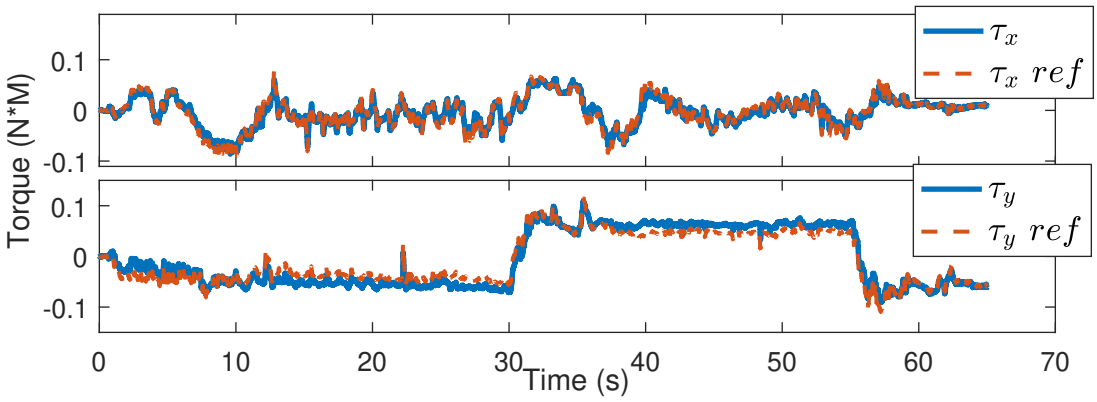

Figure 2.21: External torque profile for moving on ball environment.

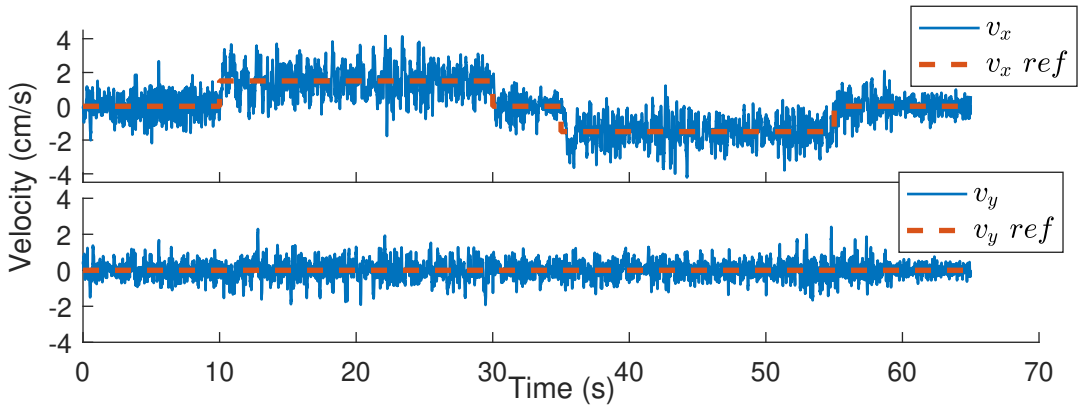

Figure 2.22: Velocity tracking for moving on ball environment.

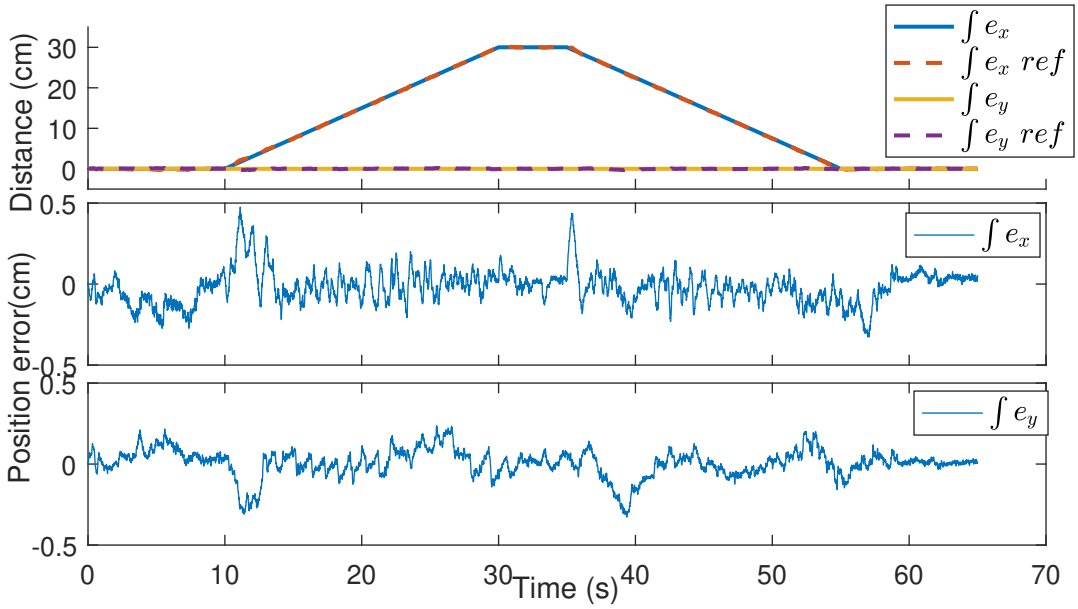

Figure 2.23: Position tracking for moving on ball environment.

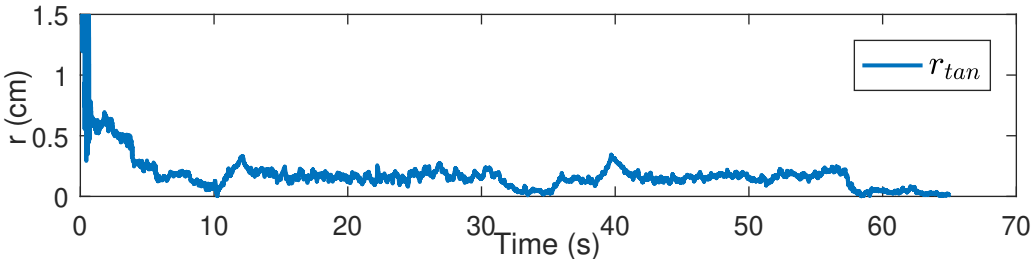

Figure 2.24: Alignment evaluation for moving on ball environment.

For the third experiment, in order to prove the proposed algorithm can achieve the real-world application, we replace the ball environment to the mannequin which is a irregular surface. From 0s-10s, we command the same force along the end-effector Z direction. Then we set $v_{dx} = 0cm/s, v_{dy} = 0.15cm/s$ for 10s-30s, $v_{dx} = 0.05cm/s, v_{dy} = 0cm/s$ for 30s-50s, $v_{dx} =$

$0\text{cm/s}, v_{dy} = 0\text{cm/s}$ for 50s-55s, then command the same velocity in opposite direction. From the Figures 2.25 - 2.29, we can see that the overall performance is not as good as the second experiment. This degradation is mainly affected by the irregular environment. When the end-effector moves toward to the sharp curve on the mannequin, such as 13s-18s, 40s-45s, 70s-73s, 88s-93s, the force tracking and position tracking and alignment was all affected. The force in end-effector z direction will goes to 4N for about 0.1s, the position error will in crease to 0.6cm, the equivalent level also increase to $1 - 1.5\text{cm}$, but all the degradation just happens in a very short period.

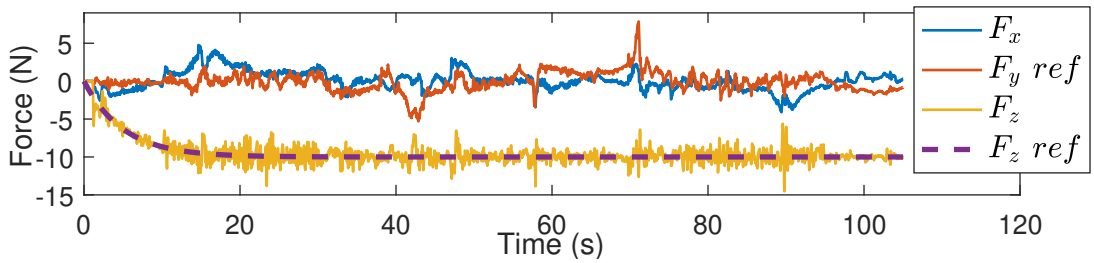

Figure 2.25: External force profile for moving on mannequin.

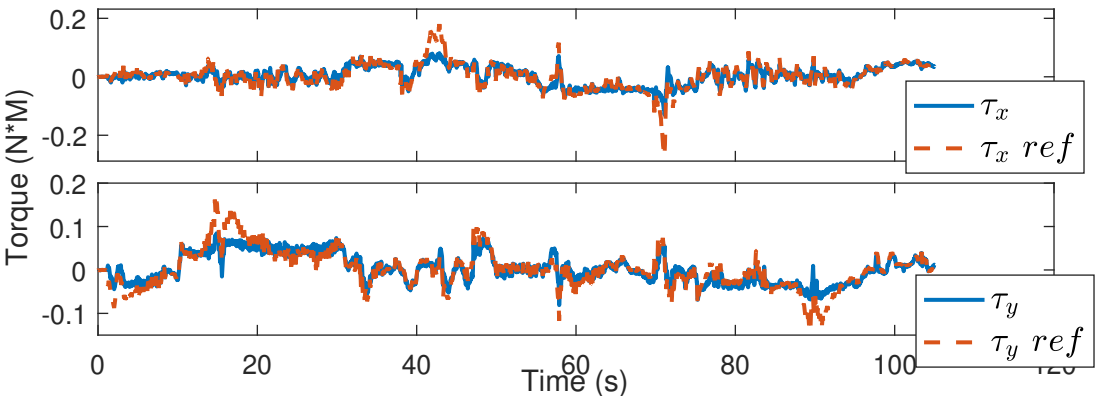

Figure 2.26: External torque profile for moving on mannequin.

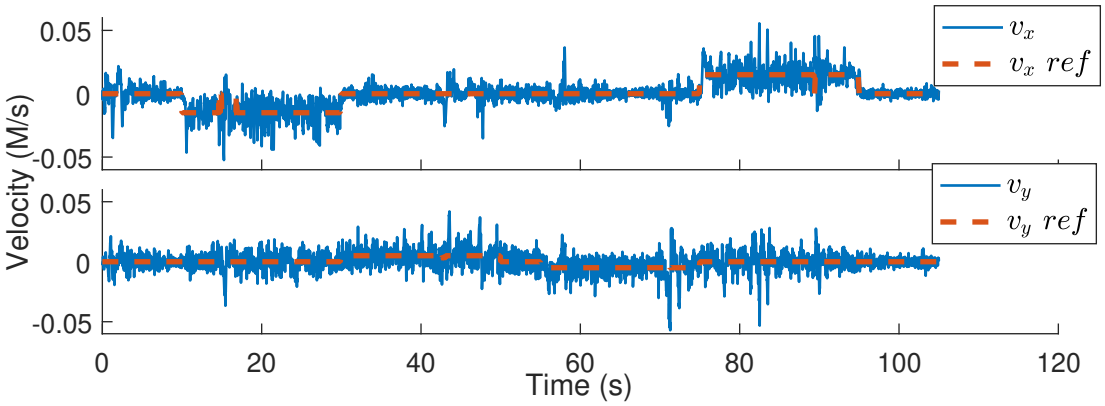

Figure 2.27: Velocity tracking for moving on mannequin.

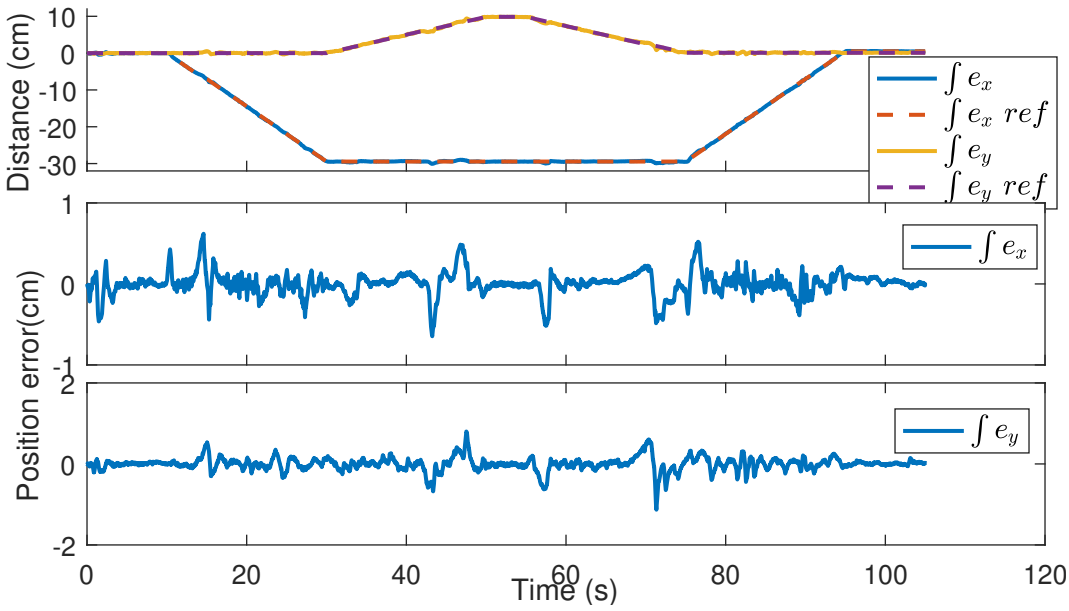

Figure 2.28: Position tracking and error profile for moving on mannequin.

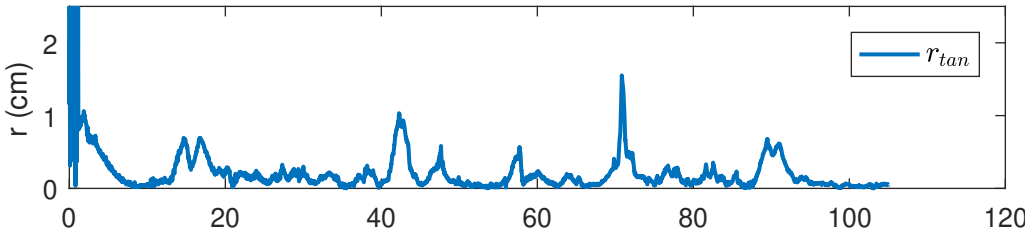

Figure 2.29: Equivalent lever in the tangential plane of end-effector.

CHAPTER 3: ADAPTIVE CONTROL BASED APPROACH FOR 1-CLICK GRIPPING NOVEL OBJECTS

Z. Ding, N. Paperno, K. Prakash and A. Behal, "An Adaptive Control-Based Approach for 1-Click Gripping of Novel Objects Using a Robotic Manipulator," in IEEE Transactions on Control Systems Technology, vol. 27, no. 4, pp. 1805-1812, July 2019.

Background and Motivation

Various slip sensors and slip prevention methods have been proposed in literature by researchers to achieve the aforementioned immobilization goal. One way to sort the approaches is by utilization of the signal used for slip detection such as pressure/force-based, vibration-based, or optical sensor-based. In [25] and [26], slip was considered to have occurred by monitoring the deviation in force from static condition over a chosen threshold or the rate of change of aforestated deviation below another chosen threshold; when slip was detected, the desired target grasp force was increased by a known amount. In [27], researchers detected the high frequency vibration of the shear force derivative to measure slip based on which a sliding mode controller was developed to estimate the grasping force. In [28], a biomimetic tactile sensor was utilized to achieve the force estimation and slip detection/classification. Slip was detected by observing change in the tangential force and slip-related micro-vibration signal from the built-in pressure sensor. In the force estimation part, machine learning techniques were used to map the raw reading from the sensor to the actual force and gripper force was adjusted by estimating the friction coefficient. In [29], pressure conductive rubber was utilized as the detection element to build a highly sensitive slip sensor. Initial slip was detected by monitoring the high frequency component of the sensor output; once initial slip

was detected, gripping force was increased proportional to the slip detection signal. In [30], a slip detection and correction strategy using a tactile sensor was devised – slip was detected by observing the covariance of different tactile sensor readings. Their force regulation considered the magnitude of the slip which could ensure that the slip is eliminated without excessive force. In [31], the performance of an optical sensor as a slip sensor was tested for different textures. In [32], an optical sensor was utilized to detect the slip and a closed-loop control system was designed to adjust the grasping force; however, only one object was tested and the amount of deformation in the object was not specified. In [33], a combined optical-mechanical tactile sensing method with high sensitivity slip detection was developed to enable fine finger-force control needed for grasping different objects in a home use manipulation system; upon detection of slip, the finger was closed by a pre-defined amount to prevent further slip.

In previous work by the authors [43], an open-loop force flatness-based adaptive algorithm was described in order to grasp a large class of novel objects involved with activities of daily living. The algorithm obviated the need for exactly calibrated force sensing because the inference was based on deviation. For the sake of completeness, we briefly describe the algorithm in what follows. Since many objects have an enclosed surface or at least some reinforcement where the surface is not enclosed, they show compliance when pushed and offer gradually increasing stiffness before yielding which leads to a characteristic flattened "hump-like" profile when the gripper is allowed to close in open-loop. This flatness in the force profile can be used as a leading indicator of the onset of the yield point and used to adaptively find a grasping force setpoint for different objects and for different states of the same object. A robust 'flatness' of force profile is assessed using a sliding-window based approach which indicates 'flatness' in a signal when the following condition is satisfied [43]

$$g(t) \triangleq \sup_{t \in [t-\Delta T, t]} \left| \frac{df(t)}{dt} \right| < \epsilon \tag{3.1}$$

where $f(t)$ denotes the interaction force, ΔT is a user-defined sliding time window width, while ϵ is a small constant which denotes numerical tolerance. While this method works for many objects, it is not effective when applied to "soft" objects such as empty paper, plastic, or Styrofoam cups which do not offer any usable flatness profile before being crushed and deformed while being grabbed. This motivates us to develop a closed-loop adaptive scheme which is applicable over a wider class of objects and is able to grasp with further reduction in deformation.

Problem Statement and Modeling

The research objective is to utilize adaptive control in order to drive a robot gripper to grasp novel objects without slippage and with minimal deformation. By embedding sensors in the gripper fingers, object slip velocity and gripper force are available to us as measurements while gripper velocity in the opening/closing direction is available as the control input. It is assumed that no information about object geometry, weight, and texture is available which implies that the disturbance force acting on the object (e.g., due to a gravity field) as well as the frictional force between the object and the gripper are unknown. As shown in Figure 3.1, consider an arbitrary object between the gripper fingers acted upon by a constant disturbance force W, applied gripper force F_a, and frictional force $F_f = \mu F_a$ where μ is the coefficient of friction between the gripper and the object such that the dynamics of the slip velocity $v(t)$ can be written as

$$m\dot{v} = W - \mu F_a. \tag{3.2}$$

Since it is not possible to directly control and apply the gripper force $F_a(t)$, we model the incremental displacement $x_g(t)$ of the gripper as proportional to the applied force such that

$$F_a \propto x_g \tag{3.3}$$

the time derivative of which can be related to the control input signal, the gripper velocity $v_g(t)$ as follows

$$\dot{F}_a = \kappa v_g. \tag{3.4}$$

Thus, (3.2) and (3.4) denote the overall system dynamics. Here, in deference to our problem statement above, W, μ,and κ are assumed to be unknown parameters which will be adapted for during the control design process.

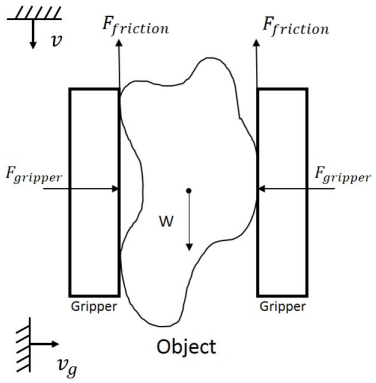

Figure 3.1: Free Body Diagram for Gripper Object Interaction

Control Design and Stability Analysis

Based on our desire to utilize an adaptive backstepping approach to the problem, we design a desired gripper force based on (3.2) as follows

$$F_d \triangleq \hat{\mu}^{-1}(\hat{W} + k_1 v) \tag{3.5}$$

where $k_1 > 0$ is a control gain, while $\hat{\mu}(t)$ and $\hat{W}(t)$ are yet to be designed parameter estimates such that the dynamics of (3.2) can be rewritten as

$$m\dot{v} = \tilde{W} - k_1 v - \tilde{\mu}\hat{\mu}^{-1}(\hat{W} + k_1 v) - \mu F_e \tag{3.6}$$

Here, $F_e(t)$ is an auxiliary variable defined as follows

$$F_e \triangleq F_a - F_d, \tag{3.7}$$

whereas $\tilde{\mu}(t), \tilde{W}(t)$ are parameter estimation errors defined as follows

$$\begin{aligned} \tilde{\mu} &\triangleq \mu - \hat{\mu} \\ \tilde{W} &\triangleq W - \hat{W} \end{aligned} \tag{3.8}$$

To motivate the design of the adaptive parameter estimation and understand the rationale behind the design of (3.5), we define a positive-definite function V_0 as follows

$$V_0 = \frac{1}{2} m v^2 + \frac{1}{2}\gamma_1^{-1}\tilde{W}^2 + \frac{1}{2}\gamma_2^{-1}\tilde{\mu}^2 \tag{3.9}$$

where γ_1 and γ_2 are positive constants. Differentiating (3.9) along the trajectory of (3.6) yields

$$\begin{aligned} \dot{V}_0 = \; & \left(\tilde{W} - k_1 v - \tilde{\mu}\hat{\mu}^{-1}(\hat{W} + k_1 v)\right) v \\ & -\gamma_1^{-1}\tilde{W}\dot{\hat{W}} - \gamma_2^{-1}\tilde{\mu}\dot{\hat{\mu}} - \mu F_e v \end{aligned} \tag{3.10}$$

which can be conveniently rearranged as follows

$$\begin{aligned} \dot{V}_0 = \; & -k_1 v^2 - \mu F_e v + \tilde{W}\left(v - \gamma_1^{-1}\dot{\hat{W}}\right) \\ & -\tilde{\mu}\left(\hat{\mu}^{-1}(\hat{W} + k_1 v)v + \gamma_2^{-1}\dot{\hat{\mu}}\right) \end{aligned} \tag{3.11}$$

Based on the structure of the parenthesized terms in (3.11), one can design adaptive estimation for $\hat{\mu}(t)$ and $\hat{W}(t)$ as follows

$$\dot{\hat{W}} \triangleq \gamma_1 v \tag{3.12}$$

$$\dot{\hat{\mu}} \triangleq -\gamma_2 \hat{\mu}^{-1}(\hat{W} + k_1 v)v \tag{3.13}$$

where we can utilize a projection algorithm (*e.g.,* see [36]) to ensure that $\hat{\mu}(t) > 0$. By substituting (4.1) and (4.2) in (3.11), we can obtain

$$\dot{V}_0 = -k_1 v^2 - \mu F_e v \tag{3.14}$$

which would be negative semi-definite if the error between the desired and actual gripper force is zero. Proceeding further with the design, one can time differentiate (3.7) to obtain the dynamics of $F_e(t)$ as follows

$$\dot{F}_e = \kappa v_g - \dot{F}_d \tag{3.15}$$

where we have utilized (3.4). Explicit time differentiation of (3.5) and elimination of the immeasurable $\dot{v}(t)$ via (3.2) yields

$$\dot{F}_d = -\dot{\hat{\mu}}\hat{\mu}^{-2}(\hat{W} + k_1 v) + \hat{\mu}^{-1}[\dot{\hat{W}} + k_1(\frac{W}{m} - \frac{\mu}{m}F_a)] \tag{3.16}$$

which can be compactly written as

$$\dot{F}_d = \dot{F}_{dm} + Y\theta \tag{3.17}$$

where $\dot{F}_{dm} = -\dot{\hat{\mu}}\hat{\mu}^{-2}(\hat{W} + k_1 v) + \hat{\mu}^{-1}\dot{\hat{W}}$ is the measurable part of $\dot{F}_d(t)$ while the immeasurable part is linearly parameterizable as $Y\theta$; here, Y is a measurable regression vector while θ denotes an

unknown parameter vector. Both these variables can be explicitly defined as follows

$$\begin{aligned} Y &\triangleq \begin{bmatrix} \hat{\mu}^{-1} k_1 & -\hat{\mu}^{-1} k_1 F_a \end{bmatrix} \\ \theta &\triangleq \begin{bmatrix} \frac{W}{m} & \frac{\mu}{m} \end{bmatrix}^T \end{aligned} \tag{3.18}$$

After substituting (3.17) into (3.15), we can design the control input $v_g(t)$ as follows

$$v_g = \hat{\kappa}^{-1}(v - k_2 F_e + Y\hat{\theta} + \dot{F}_{dm}) \tag{3.19}$$

where $k_2 > 0$ is a control gain, while $\hat{\kappa}(t)$ and $\hat{\theta}(t)$ are parameter estimates which are yet to be designed. After substituting for (3.19) into (3.15), utilizing (3.17), and rearranging terms, one can obtain the closed-loop dynamics of the force error as follows

$$\dot{F}_e = v - k_2 F_e - Y\tilde{\theta} + \tilde{\kappa}\hat{\kappa}^{-1}(v - k_2 F_e + Y\hat{\theta} + \dot{F}_{dm}) \tag{3.20}$$

where $\tilde{\kappa}(t), \tilde{\theta}(t)$ are parameter estimation errors defined as follows

$$\begin{aligned} \tilde{\kappa} &\triangleq \kappa - \hat{\kappa} \\ \tilde{\theta} &\triangleq \theta - \hat{\theta} \end{aligned} \tag{3.21}$$

To finalize the stability analysis for the overall system and motivate the design of the adaptive parameter estimation for $\hat{\kappa}(t)$ and $\hat{\theta}(t)$, we augment the function $V_0(t)$ of (3.9) to generate another positive-definite function $V(t)$ as follows

$$V = V_0 + \frac{1}{2}\mu F_e^2 + \frac{1}{2}\gamma_3^{-1}\mu\tilde{\kappa}^2 + \frac{1}{2}\gamma_4^{-1}\mu\tilde{\theta}^T\tilde{\theta}. \tag{3.22}$$

where γ_3 and γ_4 are positive constants. After differentiating (3.22) along (3.14) and (3.20), simplifying, and rearranging terms, we obtain

$$\begin{aligned} \dot{V} &= -k_1 v^2 - \mu k_2 F_e^2 + \left[-\gamma_4^{-1} \dot{\hat{\theta}}^T + Y F_e \right] \mu \tilde{\theta} \\ &\quad -\mu \tilde{\kappa} \left[\gamma_3^{-1} \dot{\hat{\kappa}} - \hat{\kappa}^{-1} (v - k_2 F_e + Y \hat{\theta} + \dot{F}_{dm}) F_e \right]. \end{aligned} \tag{3.23}$$

Motivated by the structure of the bracketed terms in (3.23), the adaptive update laws for $\hat{\kappa}(t)$ and $\hat{\theta}(t)$ can be designed as follows

$$\dot{\hat{\kappa}} = -\gamma_3 \hat{\kappa}^{-1} (v - k_2 F_e + Y \hat{\theta} + \dot{F}_{dm}) F_e, \tag{3.24}$$

$$\dot{\hat{\theta}} = \gamma_4 Y^T F_e, \tag{3.25}$$

where, as similarly done above, we can utilize a projection algorithm (*e.g.,* see [36]) to ensure that $\hat{\kappa}(t) > 0$. Substituting of (3.24) and (3.25) in (3.23) produces a negative semi-definite expression for $\dot{V}(t)$ as follows

$$\dot{V} = -k_1 v^2 - \mu k_2 F_e^2 \leq 0 \tag{3.26}$$

It is clear to see from (3.22) and (3.26) that $v(t), F_e(t) \in \mathcal{L}_2 \cap \mathcal{L}_\infty$ while $\hat{W}(t), \hat{\mu}(t), \hat{\kappa}(t), \hat{\theta}(t) \in \mathcal{L}_\infty$. Based on previous assertions, it is also clear to see from (3.6) and (3.20) that $\dot{v}(t), \dot{F}_e(t) \in \mathcal{L}_\infty$. Thus, one can utilize Barbalat's Lemma [37] [38] to prove that $\lim_{t \to \infty} v(t), F_e(t) = 0$.

Gripper Prototype Design

Implementation

Experimental Setup

The UCF-MANUS platform [35] with the newly designed gripper (as described above) was used as the experimental testbed for this paper. Empty, half and full water bottles, empty and full Styrofoam cups, empty paper cup and cereal box were used as test objects for the experiments. The full water bottle was filled with water and capped while the full Styrofoam cups were filled with sand (instead of water) to prevent any possible damage to the sensors and other electronics. For all objects, comparison was made between the gripping forces and resultant deformation when using *(a)* no algorithm, *(b)* open-loop adaptive grasping as described in Section 3, or *(c)* the proposed closed-loop adaptive grasping algorithm.

Experimental Protocol

To test gripping using the proposed closed-loop adaptive algorithm, a two-step process is utilized in which a light *initial grasp* is made followed by *adaptive regrasping* if slippage is detected upon lifting the object from its resting surface. For ease of presentation, the flowchart shown in Figure 3.2 captures the various steps involved in initial grasping and adaptive regrasping as needed.

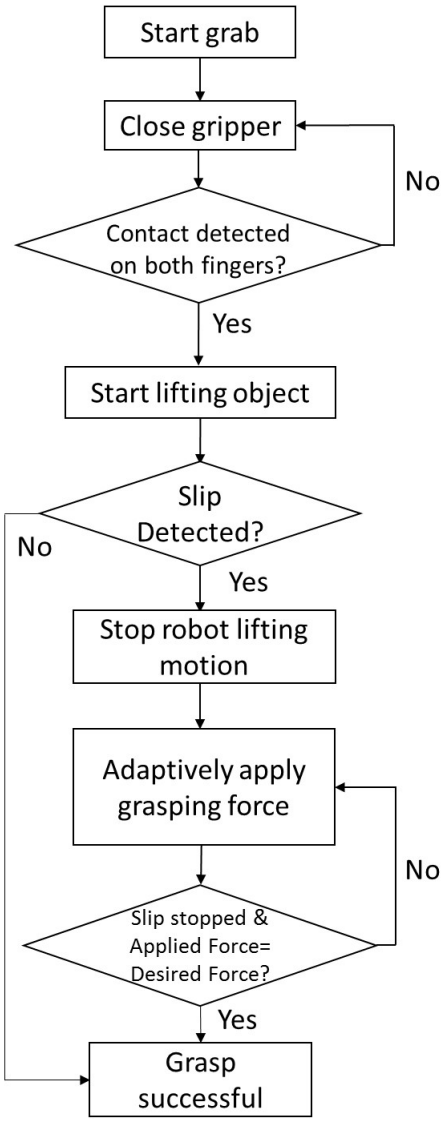

Figure 3.2: Flowchart of the proposed grasping algorithm.

Initial Grasping

Specifically, the initial grasp proceeds as follows. Since the gripper is asymmetric in terms of measurements (*i.e.,* force sensing on one side and slip sensing on the other), both the slip and force sensors are employed to ensure that both fingers are touching the object. It was determined experimentally that a force measurement of greater than $0.5\mathrm{N}$ combined with a detected slip velocity of at least $0.1\mathrm{mm/s}$ ensures a bilateral contact condition. We note here that friction between the object base and its resting surface as well as asymmetric object placement within the gripper prevents us from using just the force sensor to detect the bilateral contact condition. It is also important to note that the laser sensor, due to its high sensitivity to any displacement in its vicinity, reports low velocities which we are able to take advantage of in order to determine object contact on both gripper fingers. Once the contact condition is satisfied, the initial grasping phase concludes and an attempt is made to separate the object from its resting surface. If no slip is detected, the grasp is deemed successful and the algorithm terminates.

Adaptive Regrasping

If the force applied by initial grasping is not enough, slip will be detected which activates the adaptive regrasping controller in order to immobilize the object between the gripper fingers. In order to simplify application of the controller described in Section 3, we assume a separation of timescales and divide the controller into an outer loop which computes the setpoint for desired gripper force F_d and an inner loop which applies the appropriate gripper velocity command v_g to null the difference between F_d and the actual gripper force F_a. The simplified nested adaptive

controller can be described mathematically as follows

$$\begin{aligned} F_d &= \hat{\mu}^{-1}(\hat{W} + k_1 v) \\ \dot{\hat{W}} &\triangleq \gamma_1 v \\ \dot{\hat{\mu}} &\triangleq -\gamma_2 \hat{\mu}^{-1}(\hat{W} + k_1 v) v \\ v_g &= -k_2 (F_a - F_d) \end{aligned} \tag{3.27}$$

and can be represented in a block diagrammatic form as shown in Figure 3.3. Table 3.1 shows the values of the control gains as well as initial values of the parameter estimates. We note here that practical termination of regrasping is based on the force error being less than a small, specifiable threshold which is dependent on the available resolution of commands to the gripper.

Table 3.1: Controller Parameters

$k_1 = 1.1e3$	$k_2 = 5$
$\gamma_1 = 1e3$	$\gamma_2 = 5e1$
$\hat{W}(0) = 2$	$\hat{\mu}(0) = 2$

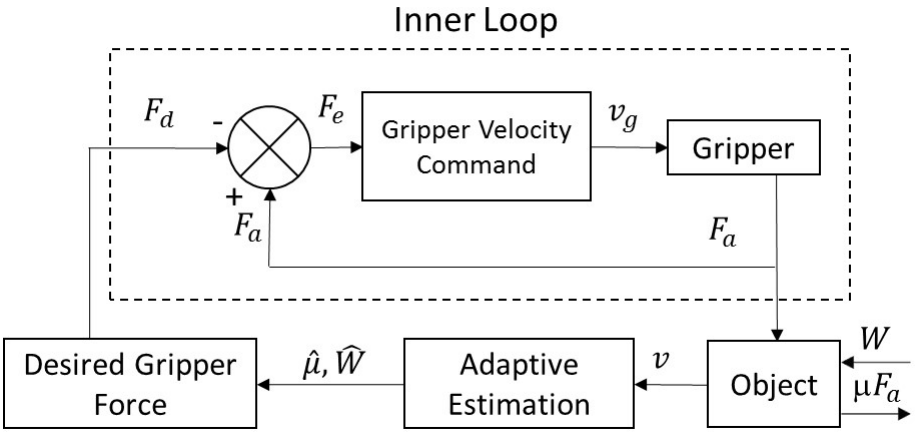

Figure 3.3: Block diagram of the simplified nested adaptive controller used for implementation.

Results

Initial Grasping

Figure 3.4 visually demonstrates the differences between no adaptation, open-loop adaptive grasping, and the proposed algorithm. As can be seen in the top row, the empty Styrofoam cups goes from being crushed ($F_a = 4N$) to medium deformation ($F_a = 2N$) to low deformation ($F_a = 1.1N$) as we move from left to right. Similar, though not as stark, differences are seen in the bottom row using a Styrofoam cup filled with sand where medium ($F_a = 9.1N$) to low ($F_a = 3.4N$) to no deformation ($F_a = 1.2N$) is observed. As expected, more gripping force is applied for the full versus empty Styrofoam cup. It is notable to observe that the state of the Styrofoam cup (whether empty or filled) is accounted for automatically by the algorithms during force application without any knowledge of such state having being provided to the gripper. Figure 3.5 shows the time evolution of force for each of the algorithms under both empty and filled cup conditions. Table 3.2 summarizes the applied force and deformation level for various objects and states under application of all three gripping schemes. In each of these cases, it is clear to see that the proposed scheme results in the least applied force resulting in slight to no deformation.

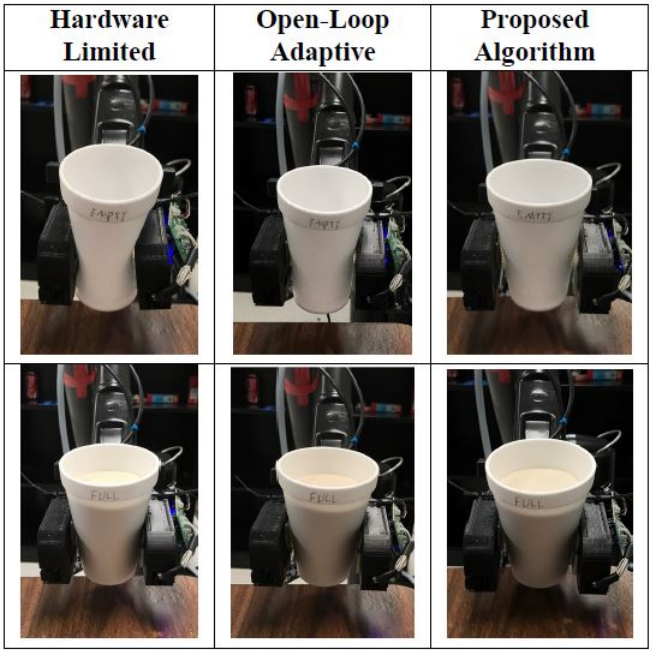

Figure 3.4: Deformation results for Styrofoam cup.

Table 3.2: Comparative force and degree-of-deformation of various objects during grasping using different algorithms

	Grasping Algorithm		
Object	**Hardware Limited**	**Open-Loop Adaptive**	**Proposed Algorithm**
EmptyWaterBottle	5.5N(high)	3.1N(medium)	1.1N(none)
EmptyFoamCup	4.0N(high)	2.0N(medium)	1.1N(low)
FullFoamCup	9.1N(medium)	3.4N(low)	1.2N(none)
EmptyPaperCup	6.0N(high)	3.1N(medium)	1.2N(low)
CerealBox	8.6N(low)	3N(low)	1.0N(none)

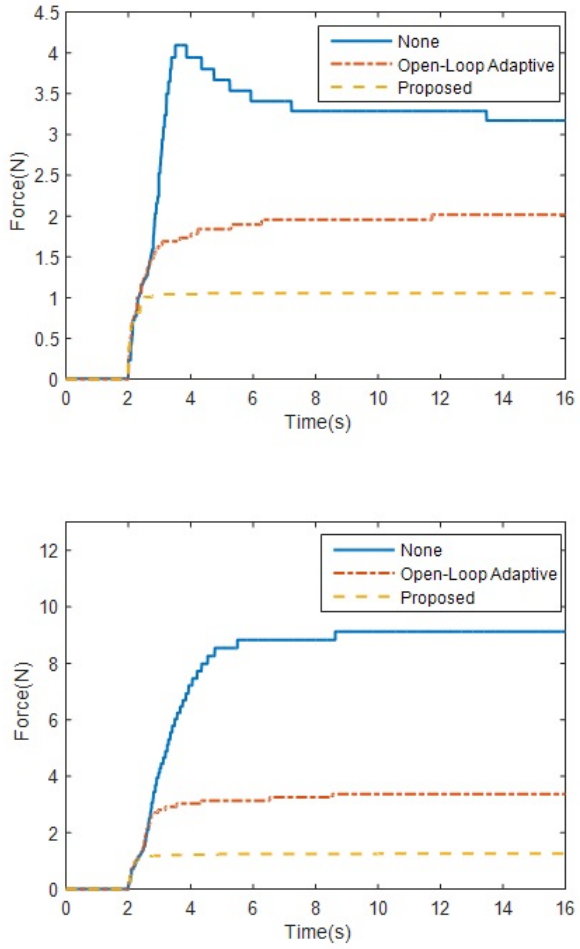

Figure 3.5: Initial Grasping Force profile for empty (top) and full (bottom) styrofoam cup.

Slip Detection and Adaptive Regrasping

While the results described above objects that could be effectively grasped using only the initial grasping portion of the proposed algorithm, this section describes results for objects that slipped during lifting after initial grasping and required adaptive regrasping. Both the half and fully filled

water bottles full were not grabbed with enough force during initial grasp resulting in slipping between the gripper fingers and the bottle during lifting. However, adaptive regrasping was employed successfully per the flowchart shown in Figure 3.2. Figure 3.6 visually demonstrates the deformation difference between aforestated algorithms**.** Figure 3.7 shows the time evolution of force for each of the algorithms for the half-filled water bottle while Figure 3.8 shows the corresponding results for the full bottle. Table 3.3 summarizes the applied force and deformation level for the half and full water bottles under application of all three gripping schemes. As can be seen moving from left to right in the table, the proposed closed-loop adaptive algorithm performs better than the open-loop adaptive algorithm which performs better than a simple hardware limited termination of gripper motion. Similarly, moving from top to bottom along the columns shows that less force is applied for the half bottle than the full bottle as expected. In Table 3.4, we show the comparison between the actual and the estimated values of the parameters W and μ. It is clear to see that W and μ are estimated very close to their actual values for the half-filled bottle but they are not quite closely estimated for the full bottle. However, our stability analysis does not provide any guarantees that these adaptive estimates will indeed converge to their actual values. However, the ratio of these two parameters gives the grasping force that gets applied to the object, and it is imperative from the practical perspective of not deforming the object that this force be close to the minimum force needed to grasp. In fact, Table 3.4 does show that the force estimated and applied by the proposed closed-loop adaptive grasping scheme compares closely with the average minimum force (determined experimentally) needed to pick up the same object, *viz.,* 1.1N (actual) versus 1.26N (estimated) for the half bottle, and 2.1N (actual) versus 2.2N (estimated) for the full bottle.

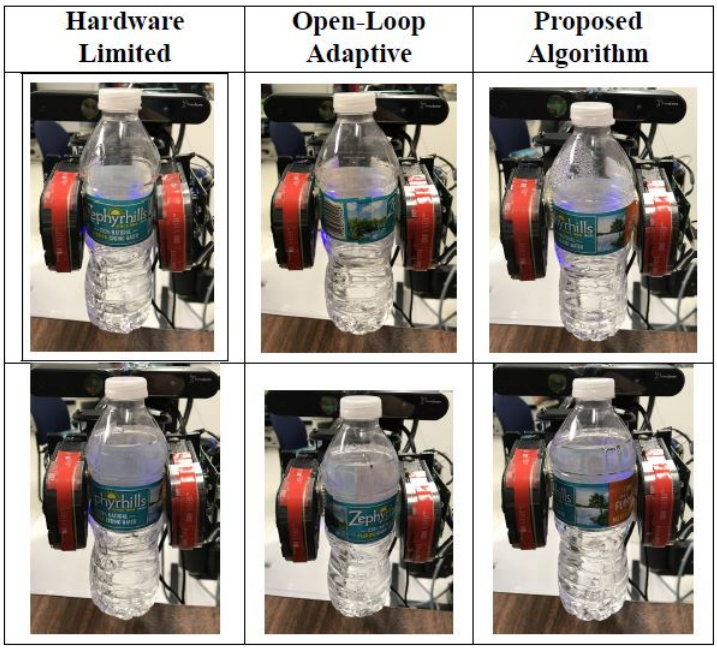

Figure 3.6: Half (top) and full WaterBottle (bottom) being grasped with no algorithm (left), open-loop adaptive grasping (middle), and proposed grasping algorithm(right).

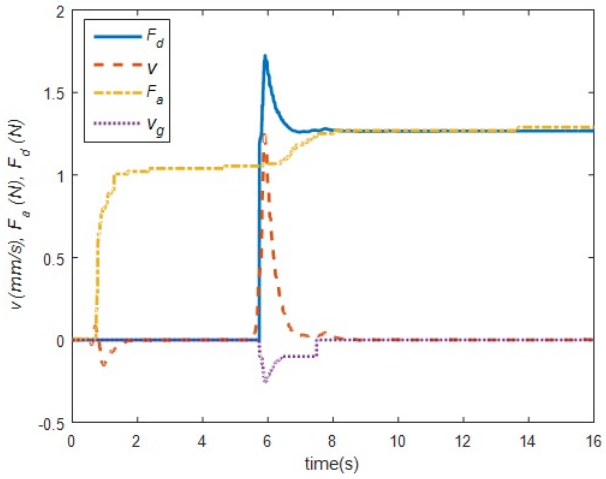

Figure 3.7: Slip detection and regrasping of half-filled water bottle.

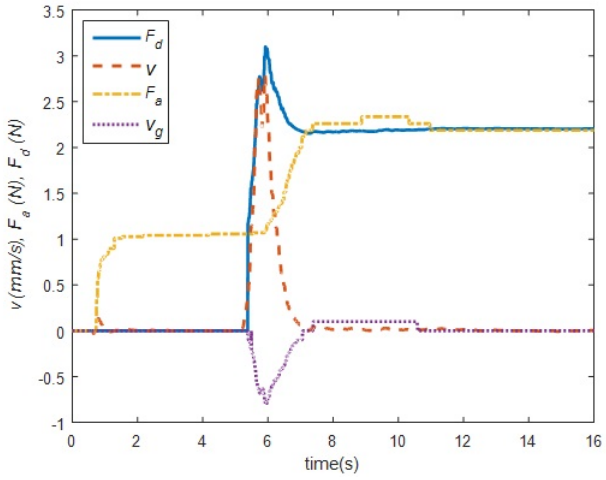

Figure 3.8: Slip detection and regrasping of fully-filled water bottle.

Table 3.3: Comparative force and degree-of-deformation of half and fully filled water bottle during grasping using different algorithms

	Grasping Algorithm		
Object	**Hardware Limited**	**Open-Loop Adaptive**	**Proposed Algorithm**
HalfWaterBottle	6.7N(high)	3.0N(medium)	1.26N(none)
FullWaterBottle	8.04N(high)	3.8N(medium)	2.2N(none)

Table 3.4: Actual and Estimated Parameter Value

	Parameters					
	Half-filled Bottle			Fully-filled Bottle		
Value	W	$\mu = F_a/W$	F_a	W	$\mu = F_a/W$	F_a
Actual	2.5N	2.27	1.1N	5.0N	2.38	2.1N
Estimated	2.48N	1.96	1.26N	3.84N	1.72	2.2N

CHAPTER 4: UCF-MANUS ASSISTIVE ROBOT SYSTEM DESIGN AND IMPLEMENTATION

Background and Motivation

Robotic assistive devices can be operated through various interface modalities, such as joysticks or touch-screens. In a robotic arm, for example, users are required to control the movement of multiple (up to 7) arm segments and the opening and closing of the gripper segment itself. Assistive technologies present usability difficulties, especially for individuals who may have upper-body, extremity, or cognitive limitations [39] [40]. To reduce the control burden of users, some researcher have addressed this problem by using automation [41] [42]. A user selects an object on a touchscreen and a robotic arm retrieves the item completely on its own. Although this eliminates some of the user limitations, previous research has shown that disabled individuals prefer to retain control over the robotic arm as they have already lost a large measure of control over their environments [43]. Completely autonomous systems are also not preferred by the users because they may be sub-optimal and/or error-prone because of technology or algorithmic limitations. Our proposed solution presents an adaptive user interface (UI) which offers multiple control modalities and compensations adjustable to each user's individual preference for level of interactivity as well as perceptual, cognitive, and physical limitations. To reduce the manual control complexity, the authors of [52] proposed a novel orientation control algorithm which is more intuitive for a broad range of users. Instead of using the original setting of the end-effector coordinate frame, the author defined an adaptive end-effector coordinate frame for generating the end-effector angular motion. Usability testing shows that the task errors and processing times are significantly lower than the original orientation control. To approach the same goal, an automatic control mode switching algorithm for the manual control of an assistive robot was proposed in [55]. Based on a

time-optimal model, they used Dijkstra's algorithm to predict when the robot should automatically change modes for the user. The authors of [54] proposed a multimodal body-machine interface for body and head-motion control for severely impaired people. A wearable and wireless body sensor network is utilized to support inertial measurement units (IMUs) and surface electromyography (sEMG) sensor nodes and also translate the upper-body gestures to control commands. There are other control modality was utilized for human-robot interaction such as through eye gaze [56] [57].

Previous research by our research group has identified some visual, cognitive, and physical abilities that can affect the performance of a user's interaction with robotic assistants [44]. Decrements in dexterity, processing speed, spatial ability, visual ability, and working memory can result in difficulty interacting with assistive technology, increased time on task, added user frustration, and decreased feelings of autonomy. The current assistive robot system offers a user-centered approach to the development of an adaptive assistive robot system. This assistive robot system aims to design compensations specifically targeted for disabled users of the system, as well as other general compensations which will benefit robot operators at large. The needs, abilities, and limitations of assistive technology users are evaluated and applied to the design of the assistive robot system, developing a system that is cognizant of the user needs and can carry out tasks effectively, safely, and with minimal physical and cognitive workload [46].

System hardware and software Architecture

Manipulator

The manipulator for our UCF-MANUS assistive robot system remains the same as the last generation [43]. It is based on the ARM (assistive robotic manipulator) manufactured by Exact Dynamics of Netherlands. It weighs ˜19 lbs. The arm is designed for wheelchair mounting and can be used

for a wide variety of tasks such as eating/drinking and picking objects from the floor. The arm can carry up to 4.5 lbs of weight in its gripper. It has 6 translational and rotational degrees of freedom that allow the robot to maintain orientation of a grasped object while bringing it back to the user. The gripper has two hinged finger tips covered with anti-slip material to allow a firm grasp of almost any object.

Sensing

For the second generation of the UCF-MANUS, we updated the sensing system on the gripper. As shown in Figure 4.1, the gripper system has several embedded sensors for vision, tactile, force, etc. For 3D vision, a PrimeSense RGB-D Camera can provide the color view of the scene to the user and a depth map for the robot system (indicating the information relating to the distance of the surfaces of scene objects from a viewpoint). 3D printed (using ABS Plastic material) frames attach around the two fingers of the bare MANUS ARM gripper. The frames were designed with appropriately sized cavities and channels for mounting and wiring various sensors. The mounted sensors include: (a) Force sensor mounted on the right finger of the gripper, providing the applied grasping force to the object; (b) LASER sensor-based slip sensor inserted in the left gripper glove for detecting the slippage between the object and the gripper [49], [50]; (c) Two sets of optical gates embedded in the glove for detecting position of object inside gripper; (d) Two sets of tactile sensors mounted along both sides of the gripper for providing collision information between the gripper and its environment.

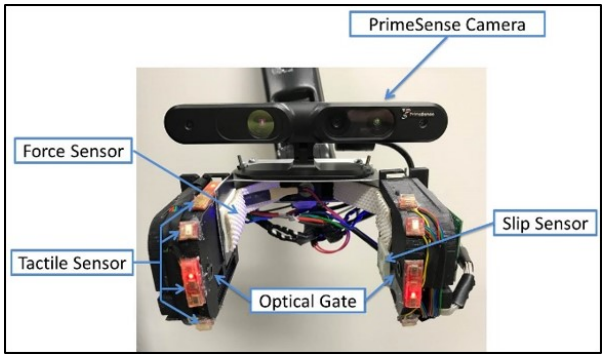

Figure 4.1: Sensor embedded gripper

Software Architecture

The overall software architecture remains the same with last generation [43]. Under the Microsoft Visual Studio integrated development environment, C/C++ language is employed to implement all the necessary software modules. Besides the compatible libraries we used for last generation, we added other libraries such as OpenNI, OpenCV2 for the video stream and better image processing. For the middleware of our system, we still using the server-client communication protocol using TCP/IP sockets. The server directly communicates with the sensing hardware as well as the GUI and the vision computational modules all of which are treated as clients. It is easy to add or remove a client without affecting the remaining components. However, since sockets-based communication requires making copies of the data packets, it is not used for high bandwidth data transfers, e.g., video frames are shared between different processes through mapped memory—thus, this data are restricted to be local to the machine with the attached visual sensing hardware.

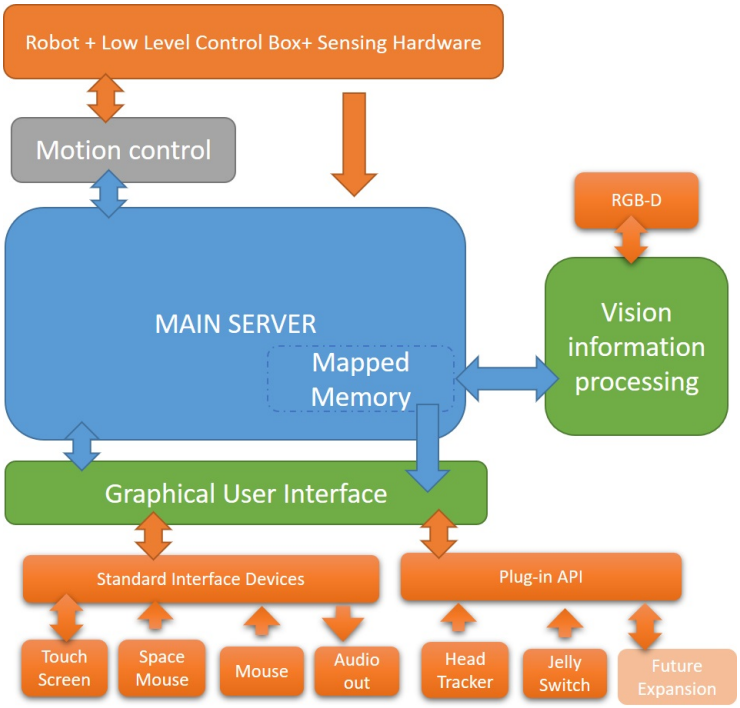

Figure 4.2: UCF-MANUS Modular System Architecture

Assistive controller design and implementation

According to our previous usability research [43], fully autonomous function ability is not appealing to the user. This motivates us to refine our human-robot interaction framework, and update our technology. Under our modified human-robot interaction framework, the user can at any time take over control of the robot. The robot will only take over the control in certain situations such as when the grasped object is slipping, and the latency inherent in transferring control to the user or seeking user permission would lead to irretrievable loss of the object from within the fingers of the gripper. The original fully manual and fully autonomous control modes available in the first-generation UCF-MANUS are now the two opposing limits for our HRI framework. With new

technology and advanced algorithms, we are able to fill the gap between the two aforementioned limits. Specifically, we design and implement the following control approach for our new HRI system.

Human-robot interaction framework

As shown in Figure 4.3, the user can control the robot via the manual control command and the assistive control command. The assistive control allows the robot's intelligent software agent take over all or part of the control, but the user still has overall supervisory control to command the robot. Furthermore, all the system events are classified as three different levels: suggested, restricted and prohibited. For the suggested events, the system will notify the user such as 'Object is in the gripper', 'Approaching to the object', etc. The restricted event include some constraint on the robot, such as 'Food may spill if gripper rolls further'. As for prohibited events, it includes collision events or physical motion limits of the robot.

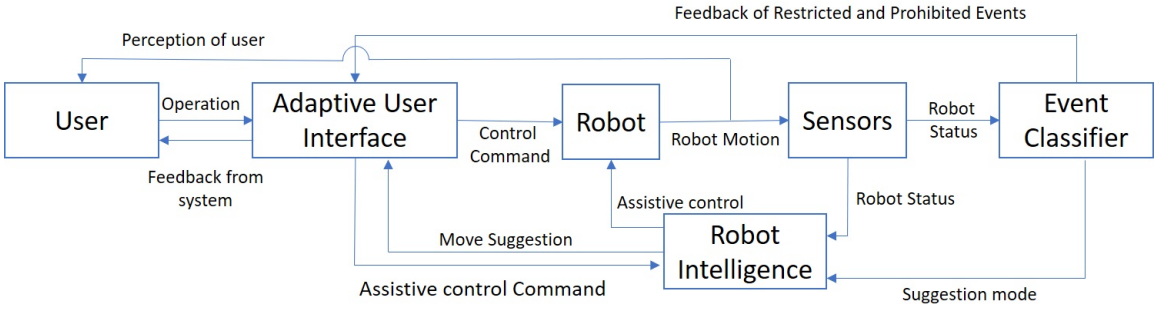

Figure 4.3: Human-robot interaction framework.

Autonomous grasping

Object Detection and Position Estimation

In our second generation UCF-MANUS assistive robot system, we utilized another novel object 6D pose estimation algorithm which is based on single 2D depth image [51]. Specifically, contact regions are determined based on edge geometric features derived from analysis of the depth map data. But the output of this algorithm is a set of graspable pairs. The user still need to manual select the grasping edge. To improved the user experience, we implemented an automatics pair selection algorithm. By scoring the feature of the edge pair candidate, we selected the highest scored edge pair to grasp.

To be specific, we defined a vector $f_i \in \mathbb{R}^{7\times 1}$ to store all the feature for each edge pair

$$f_i = \begin{bmatrix} e_{r,i} & l_{1,i} & l_{2,i} & n_{1,i} & n_{2,i} & \theta_{z,i} & \frac{\pi}{2} - \theta_{x,i} \end{bmatrix}$$

where $e_{r,i}$ is the error of the RANSAC algorithm which represents the quality of the fitted plane, $l_{1,i}$ and $l_{2,i}$ are the length of each edge, $n_{1,i}$ and $n_{2,i}$ are the pixel number of each edge, $\theta_{z,i}$ is the angle of the surface normal and z- axis of base frame, $\theta_{x,i}$ is the angle of the surface normal and x-axis of base frame.

To make all the score comparable, we defined the normalized feature vector F_i for each edge pair as follow $F_i = [e_{r,i} \;\; l_{1,i}/l_{1,max} \;\; l_{2,i}/l_{2,max} \;\; n_{1,i}/n_{1,max} \;\; n_{2,i}/n_{2,max} \;\; \theta_{z,i}/\theta_{z,max} \;\; \frac{\pi}{2} - \theta_{x,i}/\theta_{x,max}]$ where $l_{1,max}, l_{2,max}, n_{1,max}, n_{2,max}, \theta_{z,max}, \theta_{x,max}$ the max value of those feature in all the edge pair candidates. Then we will pick the highest score as the target graspable edge pair and output the estimate 6D position $\hat{X}_o = \begin{bmatrix} \hat{x}_o & \hat{\theta}_o \end{bmatrix}^T \in \mathbb{R}^{6\times 1}$ to the robot control module.

Auto Object approaching control

In this auto control mode, the system will automatically generate the motion control of the end-effector to approaching the detected object. The translation axis controller will drive the end-effector to the desired approaching position, while the rotational axis controller will keep the end-effector always pointing to the detected object.

Once we have the estimated object position and orientation $\hat{X}_o$ from the Depth image based autonomous grasping algorithm. We can define the desired approaching position as follow

$$X_d = \begin{bmatrix} x_d & \hat{\theta}_o \end{bmatrix}^T$$

where $x_d = \hat{x}_o - x_{off}\hat{n}_x, \hat{n}_x$ is the unit vector of the x- direction of the estimated object surface, x_{off} is the distance from the object surface to the desired approaching position.

For the translation motion, we used a Proportional (P) position controller; here, the position error is defined as

$$e_x = x_d - x$$

and the velocity control input is

$$v_e = V_l \frac{e_x}{|e_x|}$$

where V_l is the preset translation velocity for the end-effector.

As for the rotational axis, we designed an algorithm to generate the desired orientation for the end-effector to satisfy the FOV constraint. Then we utilized a P orientation controller to regulate the orientation of the end-effector to the desired orientation. First we can define the object position error as follows

$$e_o = \hat{x}_o - x$$

where $x \in \mathbb{R}^{6\times 1}$ is the current position and orientation. Based on the object position error e_o, we can define the desired yaw and pitch angle for the end-effector FOV constraint and the angle error as follows

$$\theta_{yd} = a\tan(\frac{e_{o,y}}{e_{o,x}})$$
$$\theta_{pd} = a\tan(\frac{e_{o,z}}{\sqrt{e_{o,x}^2+e_{o,y}^2}})$$
$$e_\theta = \begin{bmatrix} \theta_{yd}-\theta_y & \theta_{pd}-\theta_p & 0 \end{bmatrix}^T$$

then we can design the robot velocity input as follows

$$\omega_e = V_\omega \frac{e_\theta}{|e_\theta|}$$

where V_ω is the preset angular velocity for the end-effector.

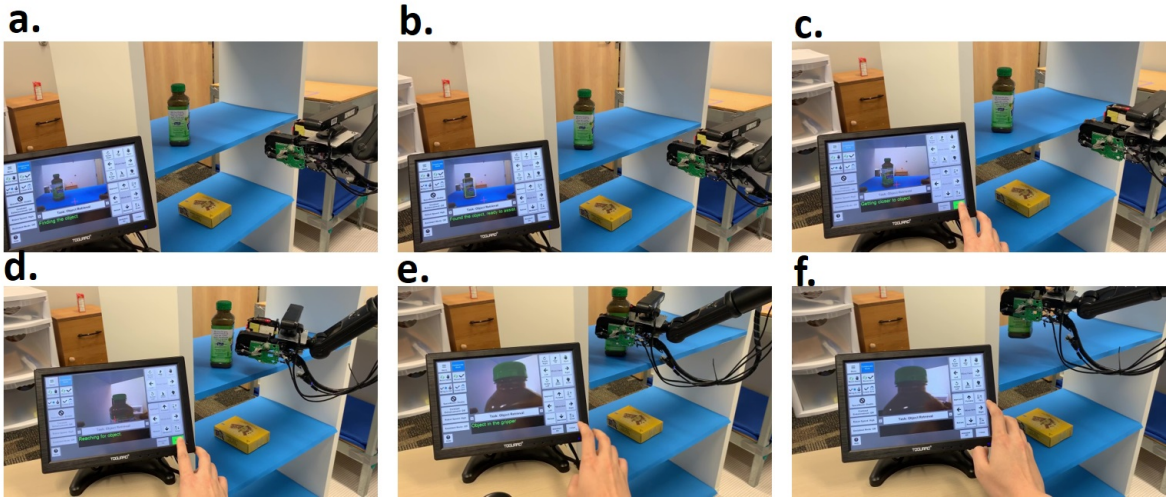

Figure 4.4: Video frames of the autonomous grasping. a) Begninning of the process, system is locating the object. b) System found the object. c) User using the 'click to approach' button to activate the autonomous motion. The gripper is reaching the object automaticaly. d) Gripper reach the pre-approaching position, Starts to approach the object. e) When the object is in the gripper, the algorithm will stop the approaching motion, and suggest user to close the gripper. f) User close the gripper and lift the object.

Robust approaching

With our last generation of robust approaching algorithm, we can only compensate the position error along the end-effector x axis. But the new object position estimation algorithm used an eye on hand system. But due to the kinematic uncertainty in the robot owing to extensive gearing and transmission, the estimated object position could has an error to the actually position. Once the system estimated the object position and drive the end-effector reach the pre-approaching position, the end-effector velocity control will only command the end-effector x axis velocity to approach

the object until the gripper sense the object is in the gripper. Since the estimated object position could contains such estimation error, then this open loop approaching process could fail, such as push the object. For this situation, embedded tactile sensors along the gripper fingers to augment our robust approaching control for tolerating position error along end-effector Y-axis also.

This algorithm will generate the adjusted pre-approaching position based on the tactile sensor feedback. Once the collision was sensed, the end-effector will retreat to the adjusted pre-approaching position and approaching again. The approaching position

$$X_d = \begin{bmatrix} x_d & \hat{\theta}_o \end{bmatrix}$$

then the adjusted approaching position can be defined as follow

$$X_{d,adj} = X_d + L_{ad}\hat{n}_{ad}$$

where $\hat{n}_{ad} \in \mathbb{R}^{6\times 1}$ is the direction of adjusting, each element was defined by the collision position. and the L_{ad} is the length of the adjusting. The velocity command of the retreat motion is defined as follow

$$\begin{aligned} v_r &= V_l \frac{e_r}{|e_r|} \\ e_r &= x_{d,adj} - x \end{aligned}$$

and the approaching velocity command is

$$v_a = V_l \hat{n}_x$$

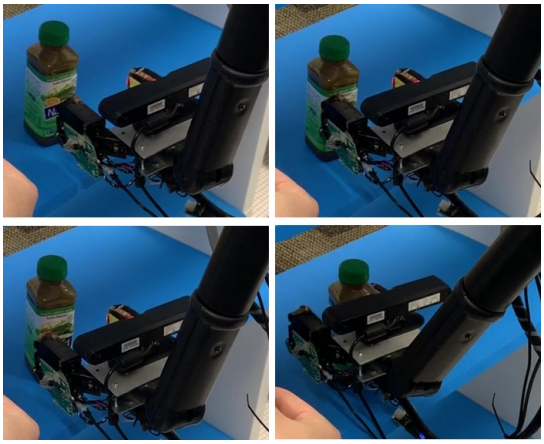

Figure 4.5: Video frames of robust approaching. Top left figure shows the estimated pre-approaching gripper position. Top right figure shows the collision between gripper and the target object. Buttom left figure shows the adjustted pre-approaching position. Buttom right figure shows the final sucess grasping.

Safe Grasping

Once the object is within the fingers of the gripper, the following process is utilized for applying the minimal force required to immobilize the object. Since ADL activities require interaction with novel objects, the exact amount of gripping force is not known in advance. If the grasping force is too little, the object may slip away; on the other hand, if the grasping force is too much, the gripper could crush the object. Based on these needs, we designed an adaptive algorithm for determining optimal grasping force [49]. This algorithm enables the robot to grasp different objects without crushing or dropping the object. By utilizing a Lyapunov-based analysis, we designed the control

law for gripper finger velocity $v_g(t)$ as follows

$$v_g = \hat{\kappa}^{-1}(v - k_2 F_e + Y\hat{\theta} + \dot{F}_{dm})$$

where $F_e \triangleq F_a - F_d$ is the grasping force error, F_a is the applied gripper force, $F_d \triangleq \hat{\mu}^{-1}(\hat{W} + k_1 v)$ is the desired grasping force, $v(t)$ is the object slip velocity, while

$$\begin{aligned} Y &\triangleq \begin{bmatrix} \hat{\mu}^{-1}k_1 & -\hat{\mu}^{-1}k_1 F_a \end{bmatrix} \\ \dot{F}_{dm} &= -\dot{\hat{\mu}}\hat{\mu}^{-2}(\hat{W} + k_1 v) + \hat{\mu}^{-1}\dot{\hat{W}} \end{aligned}$$

are auxiliary signals, while $\hat{W}(t), \hat{\mu}(t), \hat{\kappa}(t), \hat{\theta}(t)$ are parameter estimates that are dynamically updated as follows

$$\dot{\hat{W}} \triangleq \gamma_1 v \tag{4.1}$$

$$\dot{\hat{\mu}} \triangleq -\gamma_2 \hat{\mu}^{-1}(\hat{W} + k_1 v)v \tag{4.2}$$

$$\dot{\hat{\kappa}} = -\gamma_3 \hat{\kappa}^{-1}(v - k_2 F_e + Y\hat{\theta} + \dot{F}_{dm})F_e \tag{4.3}$$

$$\dot{\hat{\theta}} = \gamma_4 Y^T F_e. \tag{4.4}$$

From Figures 4.6-4.7, we can see that the proposed adaptive grasping force controller can successfully stop the slippage and regrasp target objects. A video showing the initial grasping, slip detection, and adaptive regrasping has been made available online [58].

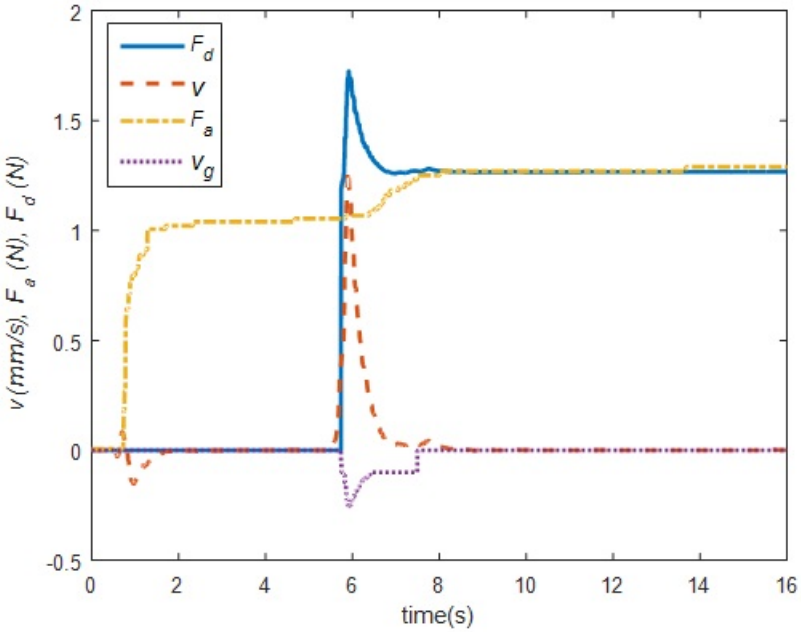

Figure 4.6: Slip detection and regrasping of half-filled water bottle. Initial grasping stage lasts between $t = 0s$ and $t = 5.4s$ using an initial grasp force of 1.05N. Robot starts lifting the bottle at $t = 5.4s$ and the algorithm detects slipping at $t = 5.7s$ at which time the proposed closed-loop adaptive algorithm activates to stop slipping using final grasping force of 1.26N.

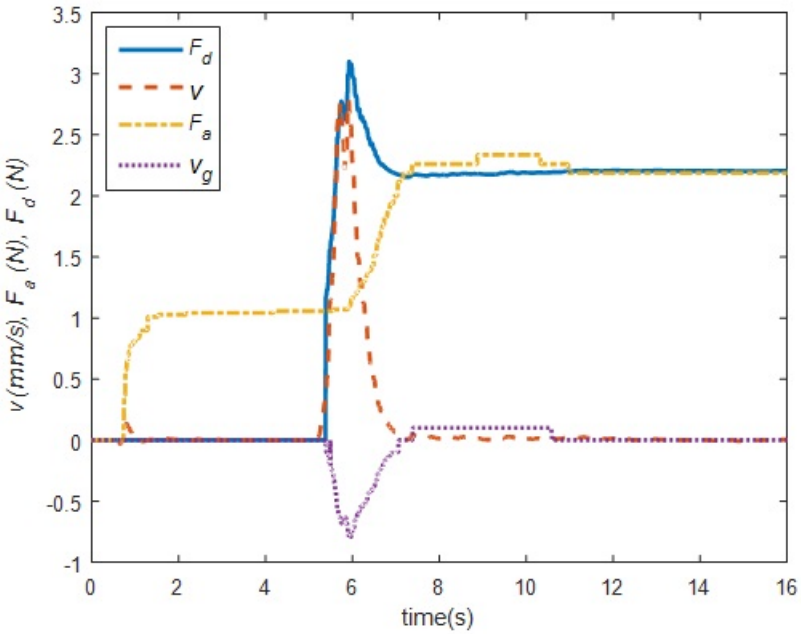

Figure 4.7: Slip detection and regrasping of fully-filled water bottle. Initial grasping stage lasts between $t = 0s$ and $t = 5s$ using an initial grasp force of 1.05N. Robot starts lifting the bottle and slipping is detected at $t = 5.7s$ at which time the proposed closed-loop adaptive algorithm activates to stop slipping using final grasping force of 2.2N.

Movement Suggestion

Besides the fully manual and fully autonomous approaching control , we also provide the user with a movement suggestion mode. Under this suggestion mode, the user still operates the robot manually, but the assistive robot system also volunteers some possible movement suggestions for the user in case they are having trouble reaching the object.

Specifically, in the suggestion mode, we define a configuration error $e_X = X - X_d$, where $X =$

$[\ x \quad \theta\ ]^T \in \mathfrak{R}^6$ is the current configuration of the end-effector. Since the user can only control one axis at each time, so the minimum operation for the end-effector to reach the desired pre-approaching position needs 6 operations. Even though the final configuration required for the robot is the desired configuration, it is possible that the object, during the movement operation, may move out of the view due to movements in a certain axis or group of axes. To keep the object always in the view, we design a finite state machine to send the suggested movement. As shown in Figure 4.8, each block represents one movement suggestion. We sort the motion in the six axes into three groups. The condition for switching to the next group/state is when the group/temporary desired position is reached. The only exception for the state changes is the collision warning. If the desired position will lead the robot arm to collide with the camera, the system will change to the next state to avoid potential collision in current axis movement. To make sure that the final position is reached in all axes, after the third group desired position is reached, the system will check for all the final desired positions having been reached or not. If not, the suggestion will switch to the first state. Otherwise the system will notify the user to manually approach the object.

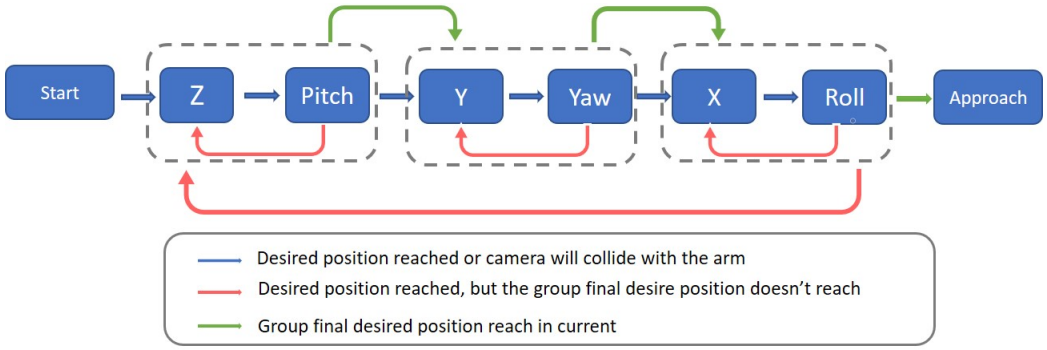

Figure 4.8: Move suggestion finite state machine. Each block represents on move suggestion, arrows indicates state transition.

To generate the desired position when the system just changes to the other state, a temporary de-

sired position will be calculated. The temporary desired position will be initialized as the final desired position. Then the system will check the object pixel position in the temporary desired position. Since we have the estimated position of the target object, we can use the camera model and camera position to calculate the pixel position of the object in the camera view. Before suggesting the motion, the algorithm will first calculate the object pixel position of the temporary waypoint $X_{d,i} = X_i - Ne_{X,i}$, where $N = diag\{x, y, z, yaw, pitch, roll\}$ is the suggested axis, the value of the suggested axis will be 1, and the rest are 0. Here $e_{X,i}$ is the position error at the beginning i^{th} iteration of the suggestion. Then we can have the object pixel position r_i, c_i as follows

$$\begin{aligned} r_i &= f_x \frac{x_{d,i}}{z_{d,i}} + o_r \\ c_i &= f_y \frac{y_{d,i}}{z_{d,i}} + o_c \end{aligned}$$

where $f_x, f_y, o_r.o_c$ are intrinsic parameters of the camera. Base on the predict object pixel position, we can determine if the object is in the view or not. If the temporary desired position $X_{d,i}$ is projected to lose the object from camera view, we define another updated temporary desired position $X_{ud,i} = X_i - Ne_{X,i}/k_c$, where $k_c \in \mathbb{N}$ is the coefficient to update the temporary desired position.

Adaptive Interface design and implementation

Since potential users include a broad set of people with disabilities, the users are likely to need different modes and levels of assistance. To adapt to different users and provide useful compensation for them, we picked some common human factors to compensate. The map between assistive function/compensation and human factors are shown in Table 4.2. Before the user operates the robot, we provide the user with a series of tests for different human factors. Then, the system automatically turns compensation features ON or OFF according to these test scores; however, the

users are able t override these choices at any time. In our adaptive UI, controls are organized by task. The UI design is shown in Figure 4.9. The right side of the display has two control boxes and two functional buttons. The upper box controls all the commands related to gripper motions, such as open/close, rotate the wrist up/down, etc. The lower box contains all the arm translational motions, such as moving forward/backward etc. The 'Assistant' button toggles the assistant system for Move Suggestions or Click to Approach compensations, but also indicates assistant status. A '1 Click' button is used to control 'Click to Approach' movement. The middle of the interface has a viewfinder for the gripper mounted camera. A black background box can provide the feedback of the system (such as 'Found the Object, ready to assist') or warning message (such as 'Environment Collision'), all the system feedback are listed in Table 4.1. On the left side of the interface are the preset arm position buttons which can provide users a quicker way to navigate the arm to one of many commonly needed positions. A SpaceMouse mode icon informs the user on the current mode of the SpaceMouse by both text and sign. The other three buttons allow for control of compensations for different human factors. The 'Contrast Enhancement' button can switch between 'off','low' and 'high' three different enhancment level. The 'Robot Speed' button can switch between 'low', 'medium', 'high', 'auto' four speed options. The 'auto' speed mode is 'Object Proximity Velocity Reduction' in 4. The 'Assistive mode' button is for the movement suggestion, user can select the 'off', 'Button only' and 'Button + Voice'. In the 'Button only mode', the system will high light the suggested movment button as a reference for the user. As for the 'Button + Voice' mode, the system will read out the suggested button once when the button is just highlighted.

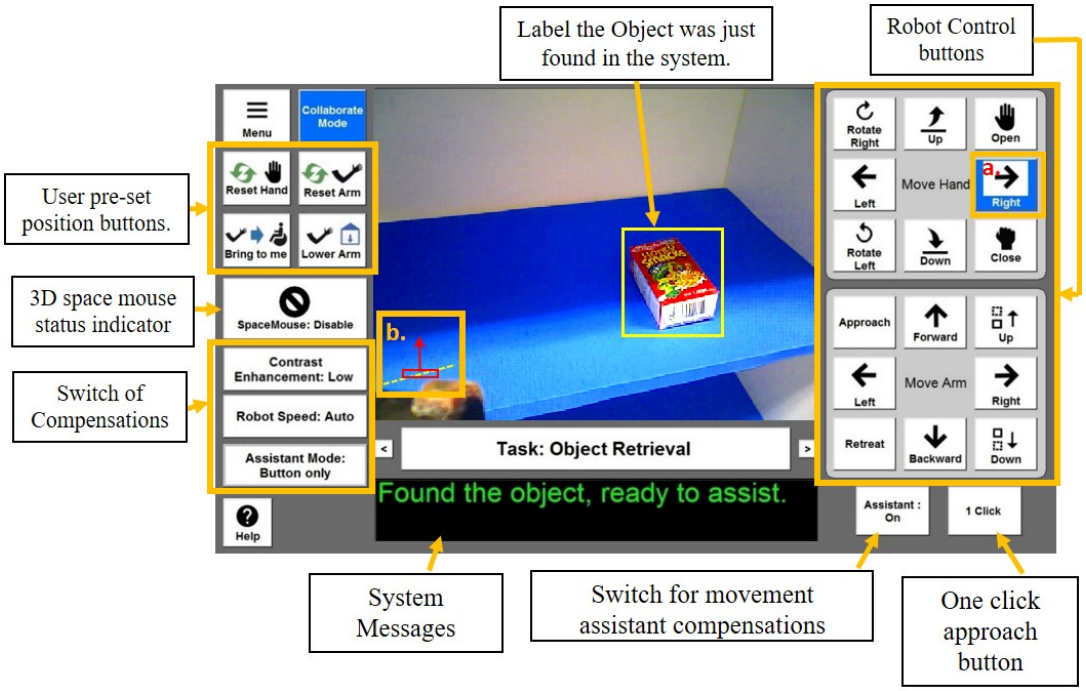

Figure 4.9: UCF-MANUS adaptive user interface

Table 4.1: List of sysem feedbacks

Evironment collision.
Camera collision.
Pitch limit reached.
Robot forward limit reached.
Robot in motion.
Finding the object.
Found the object, ready to assist.
Can’t find the object.
Object is too far away.
Getting closer to object.
Reaching for object.
Adjusting the gripper.
Please reach for object.
Object in the gripper.
Ready to lift.
Adjusting force.
Adjusting force finished.

Table 4.2: Compensation map with evaluation for deficiencies. (WM: Working Memory; RI: Response Inhibition; PS: Processing Speed; DP: Depth Perception; SA: Spatial Ability; CS: Contrast Sensitivity.) '++' and '+' stands for 'most appropriate' and 'may be useful' respectively.

	Dexterity				WM	RI	PS	DP	SA	CS
	Finger	Wrist	Arm	Head/Neck						
One-click to approach	+	+	+	++	+				+	
Safe Grasping						++	+		+	
Move Suggestion					++				++	
Orientation Indicator									++	
Object Proximity Velocity Reduction	+	++				++	++			
Contrast Enhancement										++

Contrast Enhancement

Users with visual contrast sensitivity deficiency may have difficulty perceiving objects in camera view. It could also affect the depth estimation of the user. For compensating the visual contrast sensitivity deficiency. We convert the view from RGB color space to HSV color space and then change the saturation and brightness of the picture, the brightness of the background and foreground will change, therefore enhancing the contrast of the view. As such, this compensation artificially amplifies the contrast of a scene in the UI view. Furthermore, the user has the 'low' and 'high' option for the level of enhancement. Figure 4.10 shows the view without contrast enhancement and the enhanced view.

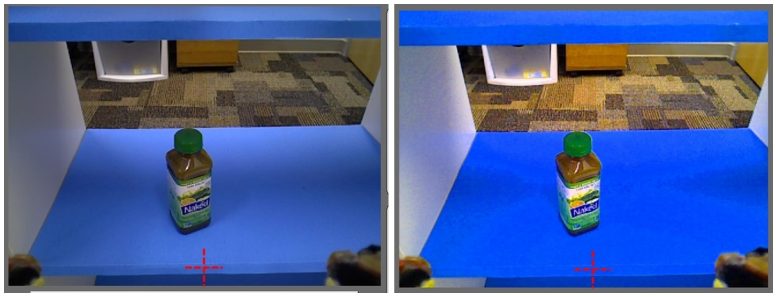

Figure 4.10: Camera view without Contrast enhancement

Object Proximity Velocity Reduction

Difficulty in motor control, as well as decreased processing speed, can lead to difficulties making the fine motor movements required near objects. To compensate, arm movement is segmented into operations requiring fine motion (close to object) and gross motion (far from objects). The arm will operate at a slower speed when it detects that it is near an object, thus allowing for greater decision and reaction time for the user. Distance from the gripper to the object is obtained from the RGB-D camera. This velocity reduction can also be selected manually; specifically, it has three speed options, namely, 'slow', 'medium', and 'high'.

Orientation indication

Users with deficient spatial orientation or visualization ability may have difficulty determining the position of the arm or gripper, including its relationship to the object they wish to manipulate. This may be magnified by an SCI user's limited dexterity and difficulty with controls. In settings with limited visual references, it may be difficult to determine the orientation of the gripper. The orientation indicator provides an artificial horizon, as well as a gripper position indicator.

Results

To test the effectiveness of these assitive modes, we tested them with pick and place task 5 times under each mode. The manual mode data is collected with an able-bodied and experienced user, so the manual mode data could be used as a benchmarkfor the upper limit of performance for a user. The comparision of all three modes of the end-to-end task is shown in Table 4.3. The end-to-end operation under one-click mode and move suggestion mode is shown in Figure 4.4 and Figure 4.11. We can see that the move suggestion mode and one-click mode both need extra time for detecting the object. But for the manual mode, we cannot simply separate the observation time during operation. So we compare the 'object detection' and 'Reaching to object' phase together. The manual mode averages 24.2s. The one-click mode averages 30s, but the move suggestion mode averages 57s. The one-click mode costs slightly more time than the manual mode, but the commands are reduced from 10 to 4. The suggestion mode costs more time, but the average total commands are similar to the manual mode. After reaching the object, the 'grasp and lift' basically cost the same time and the same number of operations. For the overall performance, the one-click time used the minimum commands and slightly more time than the manual mode, and the user has the control of the robot during the whole process. The move suggestion mode costs more time than the manual mode, but it can keep the total commands at the same level as the manual mode. It can still reduce the control complexity for the user who lacks experience or has deficits in working memory or spatial ability.

Table 4.3: Assistive mode comparison

	Object detection time	Reaching to object	Grasp and Lift	Total Time	Total Commands
Manual Mode	0s	24.2±1.4s	3.9±0.18s	28.1±4.1 s	10.6±2.4
Move Suggestion Mode	16±1.7s	41.2±0.9s	4.4±0.55s	62±2.7s	10
One-Click Mode	14±2.2s	16.7±0.5s	4.1±0.3s	34.9±2.12s	4

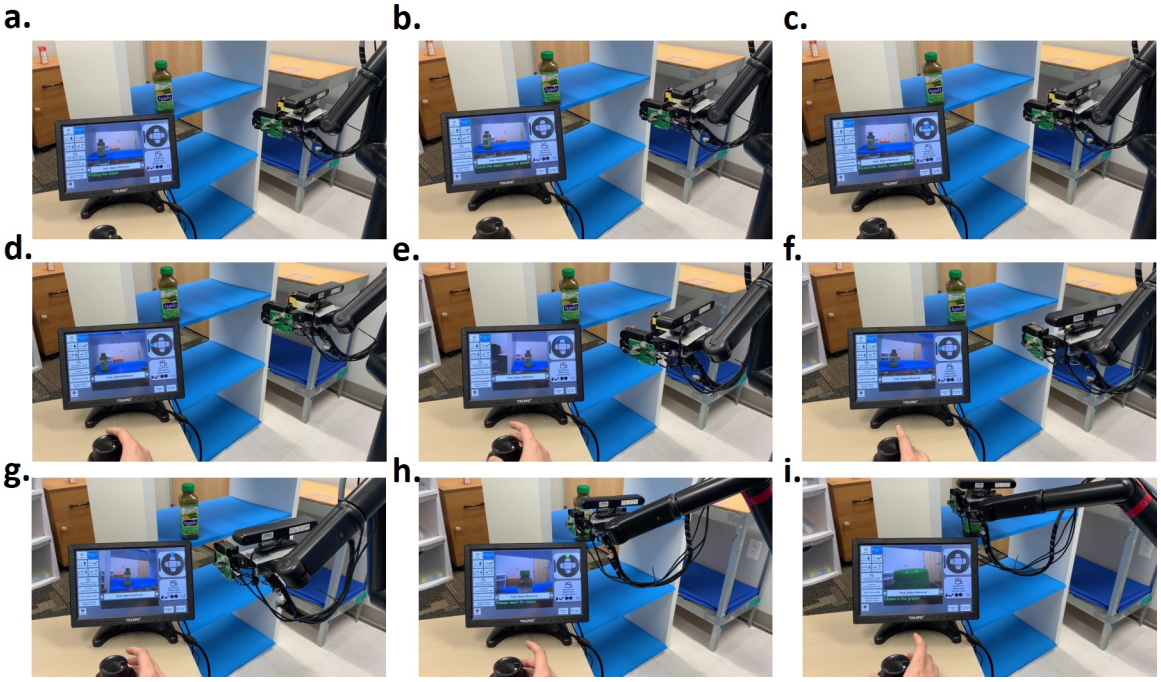

Figure 4.11: Video frames of the move suggestion mode. a) Object detection start. b) Object detected. c)Suggest move up. d) Suggest move left. e) Suggest pan right(break down the left motion to prevent object lost in the view) f) Suggest move left again. g) Suggest move forward. h) Reach to the object, user start approach to the object. i) Grasp and lift the object.

CHAPTER 5: CONCLUSION

In this dissertation proposal, two nonlinear control and one assistive robot system has been implemented for facilitating human-robot interaction. Via these assistive control, the user control complexity was reduced significantly.

For the physical human-robot interaction(P-HRI), the passive hybrid impedance control which relying on the wrist force/torque and robot joint position/velocity feedback. reduced the 6 axis control to 2 axis. Furthermore, a Lyapunov based stability analysis is provided to prove both convergence as well as passivity of the interaction to ensure both performance and safety. Simulation as well as experimental results verify the performance and robustness of the proposed impedance controller in the presence of dynamic uncertainties as well as safety compliance of physical human-robot interactions for a redundant robot manipulator.

To facilitating the control complexity of the grasping task, an intelligent single-click adaptive grasping algorithm for novel objects has been implemented relying on slip and force measurements from gripper embedded sensors. Experimental data for applied force and resultant object deformation show that the algorithm applies close to the minimal force needed to safely grasp an object without risk of slipping or excessive deformation. Comparisons are provided with an open-loop adaptive grasping algorithm as well as hardware limited grasping. Experimental results using the UCF-MANUS robotic system show that the algorithm is robust, safe, and computationally efficient. Furthermore, it is easy and inexpensive to implement on any standard gripper.

To provide user more assistive function and compensation for certain human factors, we improved our UCF-MANUS assistive robot system. the design and implementation of the assistive controller and adaptive user interface of our UCF-MANUS assistive system. All these new features are for compensating the selected human factors which cover dexterity, working memory, response inhibition, processing speed, depth perception, spatial ability, contrast sensitivity. And the results show

the assistive control mode can reduce the control complexity and also task execution time. The one-click mode reduces the operation complexity significantly while the move suggestion mode makes sure that the number of user commands matches with that for an able-bodied experienced user. However, the object detection time is higher than in the manual mode, and it consumes at least 25% of the whole processing time. This can be improved by implementing the algorithm in other programming languages or on GPU-based platforms.

APPENDIX : PROOF OF LEMMA

Proof of Linear Growth Bound of $G_1(t)$

We can also re-write the perturbation system (2.38) as follows

$$
\begin{aligned}
G_1 &= -k_e A^T H^T A v_{e,z} - k_e A^T H A v_{e,z} - k_e A^T H A A^T H^T A v_{e,z} && (.1)\\
&\quad -k_e A^T H A A^T H^T v_{xy} - k_e A^T H^T v_{xy} && (.2)\\
&\quad -A^T [\omega_e]_\times H A \frac{m_{dz}\dot{v}_{e,z} + b_{dz} v_{e,z} + f_{dz}}{A^T R_o^e A} && (.3)\\
&= -k_e A^T H^T A v_{e,z} - k_e A^T H A v_{e,z} && (.4)\\
&\quad -k_e A^T H A A^T H^T A v_{e,z} - k_e A^T H A A^T H^T v_{e,xy}\\
&\quad -k_e A^T H^T v_{e,xy} - A^T [\omega_e]_\times H A \frac{m_{dz}\dot{v}_{e,z} + b_{dz} v_{e,z} + f_{dz}}{2q_0^2 - 1}\\
&= G_{11} + G_{12} + G_{13}
\end{aligned}
$$

where $G_{11} = -A^T [\omega_e]_\times H A \frac{m_{dz}\dot{v}_{e,z}}{2q_0^2-1}$, $G_{12} = -k_e A^T H^T A v_{e,z} - k_e A^T H A v_{e,z} - k_e A^T H A A^T H^T A v_{e,z} - A^T [\omega_e]_\times H A \frac{b_{dz} v_{e,z}}{2q_0^2-1}$, $G_{13} = -k_e A^T H A A^T H^T v_{e,xy} - k_e A^T H^T v_{e,xy} - A^T [\omega_e]_\times H A \frac{f_{dz}}{2q_0^2-1}$. Since $q_0 = 1$ is exponential stable, q_0 will increasing exponentially to 1. Then we can lower bounded the denominator $2q_0^2 - 1$ by $\left\| 2q_0(0)^2 - 1 \right\|$ in G_{13}. Since $\omega_e, H \in \mathcal{L}_\infty$ and H is exponentially bounded ( ), then we can bound G_{11}, G_{12}, G_{13} as follows

$$
\begin{aligned}
& G_{11} = -A^T [\omega_e]_\times H A \frac{m_{dz}\dot{v}_{e,z}}{2q_0^2 - 1} && (.5)\\
\leq\ & \frac{m_{dz} \sup\{\|\omega_e\|\} \sup\{\|H\|\}}{\|2q_0(0)^2 - 1\|} \|\dot{v}_{e,z}\|\\
\leq\ & \gamma_1 \|\dot{v}_{e,z}\|
\end{aligned}
$$

$$
\begin{aligned}
G_{12} &= -k_e A^T H^T A v_{e,z} - k_e A^T H A v_{e,z} \qquad (.6)\\
&\quad -k_e A^T H A A^T H^T A v_{e,z} - A^T [\omega_e]_\times H A \frac{b_{dz} v_{e,z}}{2q_0^2 - 1}\\
&\leq \|k_e A^T H^T A + k_e A^T H A + k_e A^T H A A^T H^T A\\
&\quad + A^T [\omega_e]_\times H A \frac{b_{dz}}{2q_0^2 - 1}\| \, \|v_{e,z}\|\\
&\leq \gamma_2 \|v_{e,z}\|
\end{aligned}
$$

$$
\begin{aligned}
G_{13} &= -k_e A^T H A A^T H^T v_{e,xy} \qquad (.7)\\
&\quad -k_e A^T H^T v_{e,xy} - A^T [\omega_e]_\times H A \frac{f_{dz}}{2q_0^2 - 1}\\
&\leq k_e \|v_{e,xy}\|_{max} (\|H\|^2 + \|H\|) + \frac{f_{dz} \|\omega_e\|_{max}}{\|2q_0(0)^2 - 1\|} \|H\|
\end{aligned}
$$

from the proof of Lemma 2 we have $\|H\| \leq 4 \|q_m\|$, $\|H\|^2 \leq 16 \|q_m\|^2 \leq 16 \|q_m\|$, and q_m is exponentially stable, then we can have

$$
\begin{aligned}
&\leq (20 k_e \|v_{e,xy}\|_{max} + \frac{4 f_{dz} \|\omega_e\|_{max}}{\|2q_0(0)^2 - 1\|}) \|q_m\| \qquad (.8)\\
&\leq \gamma_3 e^{-\gamma t}
\end{aligned}
$$

According to (.5),(.6) and (.7), we can have the perturbation term (.1) was linear growth bounded as follow

$$
\begin{aligned}
G_1 &\leq \gamma_1 \|\dot{v}_z\| + \gamma_2 \|v_z\| + \gamma_3 e^{-\beta t} \qquad (.9)\\
&\leq \max(\gamma_1, \gamma_2, \gamma_3) \|x\|
\end{aligned}
$$

where $\gamma_1, \gamma_2, \gamma_3$ are positive constant.

Proof of Exponential boundedness of H

We defined another quaternion $q_m(q_{m0}, q_m)$ which is the quaternion represents the rotation between $\hat{n}_o, \hat{z}_e$, where $q_{m0} = \cos(\frac{\theta_m}{2}), q_m = \sin(\frac{\theta_m}{2})n$. It shares the same rotation axis n with $q(q_0, q)$, while θ_m is the misalignment angle between $\hat{n}_o, \hat{z}_e$ as shown in Figure 2.2. Based on (2.26) and $\|q\| \leq \|q(0)\| e^{-\gamma t}$, we can have $\left\|\sin(\dot{\theta}_m)\right\| \leq \left\|\sin(\dot{\theta}_m(0))\right\| e^{-\gamma t}$, and $\|\sin(\theta_m)\| = \frac{\left\|\sin(\dot{\theta}_m)\right\|}{k} \leq \frac{\left\|\sin(\dot{\theta}_m(0))\right\|}{k} e^{-\gamma t}$, then we have q_m is also bounded exponentially, such that $\lim_{t\to\infty} q_m = 0$, $\lim_{t\to\infty} q_{m0} = 1$, $\lim_{t\to\infty} R_o^e = I$. Based on $q_m(q_{m0}, q_m)$ we can have the rotation matrix between object frame and end-effector frame $R_o^e(q_{m0}, q_m) = I + H$, where $H = -2q_m^T q_m I + 2q_m q_m^T - 2q_{m0}[q_m]_\times$. Then we can bounded H as follow

$$\begin{aligned} H &= -2q_m^T q_m I + 2q_m q_m^T - 2q_{m0}[q_m]_\times \\ &\leq 4\|q_m\|^2 \\ &\leq 4\|q_m\| \end{aligned} \tag{.10}$$

Then we can have H is also exponentially bounded.

Proof of Exponential boundedness of H_2

Since we normalized the $\|r_d\|$ and $\|r_e\|$ in last section, Then the rotation R_o^e between the end-effector frame and the object frame can't be expressed with quaternion error $e(e, e_0)$. Then we define another quaternion $q_m(q_m, q_{m0})$ to represent the rotation between $\hat{n}_o$ and $\hat{z}_e$. $q_m = \sin(\frac{\theta_m}{2})n_m, q_{m0} = \cos(\frac{\theta_m}{2}), n_m = \frac{r_e \times r_d}{\|r_e \times r_d\|}$ where θ_m is the angle between $\hat{n}_o$ and $\hat{z}_e$,

Since we have e, e_0 are exponential stable, based on the equation between $\dot{\theta}_c, \dot{\theta}_d$ and θ_c, θ_d, we can also have θ_c will also converge to θ_d exponentially, then we define θ_e to represents the angle between r_e and r_d as shown in Figure 2.9, then we also have $\|\theta_e\| \leq b\exp(-\gamma t)$, since $\theta_e = \theta_o + \theta_m = f(\theta_m)\theta_m$, $f(0) = 0$, then we can have $\|\theta_m\| \leq \|\theta_e\| \leq b\exp(-\gamma t)$. Then we have q_m, q_{m0} are also exponential stable at the equilibrium ($q_m = 0, q_{m0} = 1$), so we have the $R_o^e(q_m, q_{m0}) =$

$I + H_2$ will converge to I exponentially fast, and $\|H_2\|$ is also bounded exponentially similar with the case in Lemma 2.0.2.

LIST OF REFERENCES

[1] J. Engelberger, *Robotics in Service*, Cambridge, Massachusetts, The MIT Press, 1989.

[2] H. H. Kwee, J. J. Duimel, J. J. Smits, A. A. Tuinhof de Moed, and J. A. van Woerden, "The MANUS Wheelchair-Borne Manipulator: System Review and First Results", *Proc. IARP Workshop on Domestic and Medical & Healthcare Robotics*, Newcastle, 1989.

[3] M. Van der Loos, S. Michalowski, and L. Leifer, "Design of an Omnidirectional Mobile Robot as a Manipulation Aid for the Severely Disabled", *Interactive Robotic Aids, World Rehabilitation Fund Monograph #37 (R. Foulds ed.)*, New York, 1986.

[4] R. M. Mahoney, "The Raptor Wheelchair Robot System", *Integration of Assistive Technology in the Information Age (M. Mokhtari, ed.)*, IOS, Netherlands, pp.135-141, 2001.

[5] S. D. Prior, "An electric wheelchair mounted robotic arm – a survey of potential users," *J. Med. Eng. Technology*, 14:143-154, 1990.

[6] H. Nguyen, C. Anderson, A. Trevor, A. Jain, Z. Xu, and C. Kemp, "El-E: An Assistive Robot that Fetches Objects from Flat Surfaces", *Human-Robot Interaction 2008 Workshop on Robotic Helpers*, Amsterdam, Netherlands, March 2008.

[7] Z. Bien, D.-J. Kim, M.J. Chung, D.S. Kwon, and P.H. Chang, "Development of a Wheelchair-Based Rehabilitation Robotic System (KARES II) with Various Human Robot Interaction Interfaces for the Disabled", *Proc. IEEE/ASME Int. Conf. on Advanced Intelligent Mechatronics*, pp. 902-907, July 2003.

[8] H. Neveryd and G. Bolmsj, "WALKY, an Ultrasonic Navigating Mobile Robot for the Disabled", *Proc. TIDE*, pp. 366-370, Paris, France, 1995.

[9] P. Dario, E. Guglielmelli, C. Laschi, and G. Teti, “Movaid: A Mobile Robotic System Residential Care to Disabled and Elderly People”, *The First MobiNet Symposium*, 1997.

[10] R. Bischoff, “Design, Concept, and Realization of the Humanoid Service Robot HERMES”, in *A. Zelinsky, editor, In Field and Service Robotics*, Springer, London, pp. 485-492, 1998.

[11] Ding, Z., Paperno, N., Prakash, K., & Behal, A. (2018). An Adaptive Control-Based Approach for 1-Click Gripping of Novel Objects Using a Robotic Manipulator. IEEE Transactions on Control Systems Technology, (99), 1-8.

[12] D. Kim, Z. Wang and A. Behal, ”Motion Segmentation and Control Design for UCF-MANUS—An Intelligent Assistive Robotic Manipulator,” in IEEE/ASME Transactions on Mechatronics, vol. 17, no. 5, pp. 936-948, Oct. 2012.

[13] F. Nagata, T. Hase, Z. Haga, M. Omoto, and K. Watanabe, CAD/CAMbased Position/Force Controller for a Mold Polishing Robot, Mechatronics, vol. 17, no. 4–5, pp. 207–216, 2007.

[14] C. King, T. L. Chen, A. Jain and C. C. Kemp, ”Towards an assistive robot that autonomously performs bed baths for patient hygiene,” 2010 IEEE/RSJ International Conference on Intelligent Robots and Systems, Taipei, 2010, pp. 319-324.

[15] Hawkins, K. P., King, C. H., Chen, T. L., & Kemp, C. C. (2012, September). Informing assistive robots with models of contact forces from able-bodied face wiping and shaving. In RO-MAN, 2012 IEEE (pp. 251-258). IEEE.

[16] R. S. Jamisola, P. Kormushev, A. Bicchi and D. G. Caldwell, ”Haptic exploration of unknown surfaces with discontinuities,” 2014 IEEE/RSJ International Conference on Intelligent Robots and Systems, Chicago, IL, 2014, pp. 1255-1260.

[17] L. Gracia, J. E. Solanes, P. Muz-Benavent,J. V. Miro, C. Perez-Vidal, J. Tornero, (2018). Adaptive Sliding Mode Control for Robotic Surface Treatment Using Force Feedback. Mechatronics, 52, 102-118.

[18] L. Roveda, F. Vicentini and L. M. Tosatti, "Deformation-tracking impedance control in interaction with uncertain environments," 2013 IEEE/RSJ International Conference on Intelligent Robots and Systems, Tokyo, 2013, pp. 1992-1997.

[19] V. Mallapragada, D. Erol and N. Sarkar, "A New Method of Force Control for Unknown Environments," 2006 IEEE/RSJ International Conference on Intelligent Robots and Systems, Beijing, 2006, pp. 4509-4514.

[20] J. Moura, W. Mccoll, G. Taykaldiranian, T. Tomiyama and M. S. Erden, "Automation of Train Cab Front Cleaning With a Robot Manipulator," in IEEE Robotics and Automation Letters, vol. 3, no. 4, pp. 3058-3065, Oct. 2018.

[21] A. Tayebi and S. McGilvray, "Attitude stabilization of a VTOL quadrotor aircraft," in IEEE Transactions on Control Systems Technology, vol. 14, no. 3, pp. 562-571, May 2006.

[22] H. K. Khalil, Nonlinear Systems. New York: Macmillan, 1992.

[23] Y. Hong, J. Hu, and L. Gao, "Tracking control for multi-agent consensus with an active leader and variable topology," Automatica, vol. 42, no. 7, pp. 1177–1182, 2006.

[24] D.-J. Kim, Z. Wang, and A. Behal, "Motion Segmentation and Control Design for UCF-MANUS - An Intelligent Assistive Robotic Manipulator," *IEEE/ASME Transactions on Mechatronics*, vol. 17, no. 5, pp. 936-948, Sep. 2012.

[25] H. Hasegawa, Y. Mizoguchi, K. Tadakuma, A. Ming, M. Ishikawa, and M. Shimojo, "Development of intelligent robot hand using proximity, contact and slip sensing," in *Proc. IEEE Int. Conf. Robot. Autom.*, May 2010, pp. 777–784.

[26] D. Gunji, T. Araki, A. Namiki, A. Ming, and M. Shimojo, "Grasping force control of multi-fingered robot hand based on slip detection using tactile sensor," *Journal of the Robotics Society of Japan*, vol. 25, no. 6, pp. 970-978, 2007.

[27] E. Engeberg and S. Meek, "Adaptive sliding mode control for prosthetic hands to simultaneously prevent slip and minimize deformation of grasped objects," *IEEE/ASME Trans. Mechatronics*, vol. 18, no. 1, pp. 376-385, Feb. 2013.

[28] Zhe Su, K. Hausman, Y. Chebotar, A. Molchanov, G.E. Loeb, G.S. Sukhatme, and S. Schaal, "Force estimation and slip detection/classification for grip control using a biomimetic tactile sensor," in *2015 IEEE-RAS 15$^{\text{th}}$ International Conference on Humanoid Robots (Humanoids)*, pp. 297-303, 2015.

[29] S. Teshigawara, T. Tsutsumi, S. Shimizu, Y. Suzuki, A. Ming, M. Ishikawa, and M. Shimojo, "Highly Sensitive Sensor for Detection of Initial Slip and Its Application in a Multi-fingered Robot Hand," *Proc. IEEE Int. Conf. on Robotics and Automation*, pp.1097-1102, 2011

[30] M. Stachowsky, T. Hummel, M. Moussa, and H.A. Abdullah, "A slip detection and correction strategy for precision robot grasping," *IEEE/ASME Transactions on Mechatronics,* vol. 21, no. 5, pp. 2214-2226, Oct. 2016.

[31] H. Sani and S. Meek, "Characterizing the performance of an optical slip sensor for grip control in a prosthesis," in *Proc. IEEE/RSJ Int. Conf. Intell. Robots Syst.*, pp. 1927–1932, Sep. 2011.

[32] L. Roberts, G. Singhal, and R. Kaliki, "Slip detection and grip adjustment using optical tracking in prosthetic hands," *2011 Annual International Conference of the IEEE Engineering in Medicine and Biology Society*, 2011.

[33] M. Saen, K. Ito, and K. Osada , "Action-Intention-Based Grasp Control With Fine Finger-Force Adjustment Using Combined Optical-Mechanical Tactile Sensor," *IEEE Sensors Journal*, vol. 14, no.11, pp. 4026-4033, Nov. 2014

[34] R.G. Brown, *Smoothing, Forecasting and Prediction of Discrete Time Series*, Prentice Hall, Inc: Englewood Cliffs, NJ, 1963.

[35] D.-J. Kim, Z. Wang, N. Paperno, and A. Behal, "System Design and Implementation of UCF-MANUS—An Intelligent Assistive Robotic Manipulator," in *IEEE/ASME Transactions on Mechatronics*, vol.19, no.1, pp.225-237, Feb. 2014.

[36] P. M. Patre, W. MacKunis, C. Makkar, W. E. Dixon, "Asymptotic Tracking for Uncertain Dynamic Systems via a Multilayer NN Feedforward and RISE Feedback Control Structure," *IEEE Transactions on Control Systems Technology*, vol. 16, no. 2, pp. 373–379, 2008.

[37] A. Behal, W. E. Dixon, D. M. Dawson, and B. Xian, *Lyapunov-Based Control of Robotic Systems*, CRC Press, December 17, 2009, ISBN 0-8493-7025-6.

[38] J.J.E. Slotine and W. Li, *Applied Nonlinear Control*, Prentice Hall, Inc: Englewood Cliffs, NJ, 1991.

[39] N. M. Crewe, and J. S. Krause, "Spinal cord injury," Medical, psychosocial and vocational aspects of disability. Athens: Elliott and Fitzpatrick, pp. 289-304, 2009.

[40] M. L. Cohen, D. S. Tulsky, J. A. Holdnack, N. E. Carlozzi, A. Wong, S. Magasi, R. K. Heaton, and A. W. Heinemann, "Cognition among community-dwelling individuals with spinal cord injury," Rehabilitation psychology, vol. 62, no. 4, pp. 425, 2017.

[41] K. M. Tsui, D.-J. Kim, A. Behal, D. Kontak, and H. A. Yanco, ""I want that": Human-in-the-loop control of a wheelchair-mounted robotic arm," Applied Bionics and Biomechanics, vol. 8, no. 1, pp. 127-147, 2011.

[42] K. Tsui, H. Yanco, D. Kontak, and L. Beliveau, ”Development and evaluation of a flexible interface for a wheelchair mounted robotic arm.” pp. 105-112.

[43] D.-J. Kim, R. Hazlett-Knudsen, H. Culver-Godfrey, G. Rucks, T. Cunningham, D. Portee, J. Bricout, Z. Wang, and A. Behal, “How autonomy impacts performance and satisfaction: Results from a study with spinal cord injured subjects using an assistive robot,” IEEE Transactions on Systems, Man, and Cybernetics-Part A: Systems and Humans, vol. 42, no. 1, pp. 2-14, 2012.

[44] N. Paperno, M. Rupp, E. M. Maboudou-Tchao, J. A.-A. Smither, and A. Behal, “A Predictive Model for Use of an Assistive Robotic Manipulator: Human Factors Versus Performance in Pick-and-Place/Retrieval Tasks,” IEEE Transactions on Human-Machine Systems, vol. 46, no. 6, pp. 846-858, 2016.

[45] D. W. Hess, J. H. Marwitz, and J. S. Kreutzer, “Neuropsychological impairments after spinal cord injury: A comparative study with mild traumatic brain injury,” Rehabilitation Psychology, vol. 48, no. 3, pp. 151, 2003.

[46] M. S. Sanders, and E. J. McCormick, Human factors in engineering and design: McGRAW-HILL book company, 1993.

[47] H. Kwee, J. Quaedackers, E. v. d. Bool, L. Theeuwen, and L. Speth, “Adapting the control of the MANUS manipulator for persons with cerebral palsy: An exploratory study,” Technology and Disability, vol. 14, no. 1, pp. 31-42, 2002.

[48] H. A. Tijsma, F. Liefhebber, and J. L. Herder, ”Evaluation of new user interface features for the manus robot arm.” pp. 258-263.

[49] Z. Ding, N. Paperno, K. Prakash and A. Behal, ”An Adaptive Control-Based Approach for 1-Click Gripping of Novel Objects Using a Robotic Manipulator,” in IEEE Transactions on Control Systems Technology, vol. 27, no. 4, pp. 1805-1812, July 2019.

[50] M. Al-Mohammed, Z. Ding, P. Liu and A. Behal, ”An Adaptive Control Based Approach for Gripping Novel Objects with Minimal Grasping Force,” 2018 IEEE 14th International Conference on Control and Automation (ICCA), Anchorage, AK, pp. 1040-1045, 2018.

[51] A. Jabalameli, A. Behal, ”From Single 2D Depth Image to Gripper 6D Pose Estimation: A Fast and Robust Algorithm for Grabbing Objects in Cluttered Scenes.” Robotics, no. 3: 63, 2019.

[52] D. Vu, U. C. Allard, C. Gosselin, F. Routhier, B. Gosselin and A. Campeau-Lecours, ”Intuitive adaptive orientation control of assistive robots for people living with upper limb disabilities,” 2017 International Conference on Rehabilitation Robotics (ICORR), London, 2017, pp. 795-800.

[53] T. L. Chen et al., ”Robots for humanity: using assistive robotics to empower people with disabilities,” in IEEE Robotics & Automation Magazine, vol. 20, no. 1, pp. 30-39, March 2013. doi: 10.1109/MRA.2012.2229950

[54] C. L. Fall et al., ”A Multimodal Adaptive Wireless Control Interface for People With Upper-Body Disabilities,” in IEEE Transactions on Biomedical Circuits and Systems, vol. 12, no. 3, pp. 564-575, June 2018.

[55] L. V. Herlant, R. M. Holladay and S. S. Srinivasa, ”Assistive teleoperation of robot arms via automatic time-optimal mode switching,” 2016 11th ACM/IEEE International Conference on Human-Robot Interaction (HRI), Christchurch, pp. 35-42, 2016.

[56] R. M. Aronson, T. Santini, T. C. Kler, E. Kasneci, S. Srinivasa, H. Admoni, ”Eye-hand behavior in human-robot shared manipulation.” Proceedings of the 2018 ACM/IEEE International Conference on Human-Robot Interaction. ACM, 2018.

[57] H. Admoni, A. Dragan, S. S. Srinivasa and B. Scassellati, ”Deliberate Delays During Robot-to-Human Handovers Improve Compliance With Gaze Communication,” 2014 9th ACM/IEEE International Conference on Human-Robot Interaction (HRI), Bielefeld, pp. 49-56, 2014.

[58] http://ece.ucf.edu/~abehal/AssistiveRobotics/videos/Grasping_demo.mp4